AGU PUBLICATIONS

JGR

Journal of Geophysical Research: Oceans

RESEARCH ARTICLE

10.1002/2014JC010206

Interannual variability of the surface summertime eastward jet in the South China Sea

Yuanlong Li[1], Weiqing Han[1], John L. Wilkin[2], Weifeng G. Zhang[3], Hernan Arango[2], Javier Zavala-Garay[2], Julia Levin[2], and Frederic S. Castruccio[4]

[1]Department of Atmospheric and Oceanic Sciences, University of Colorado, Boulder, Colorado, USA, [2]Institute of Marine and Coastal Sciences, Rutgers University, New Brunswick, New Jersey, USA, [3]Department of Applied Ocean Physics and Engineering, Woods Hole Oceanographic Institution, Woods Hole, Massachusetts, USA, [4]Climate and Global Dynamics Division, National Center for Atmospheric Research, Boulder, Colorado, USA

Key Points:
- The SEJ has strong interannual variations in strength and position
- SEJ variability is related with a SSH anomaly dipole
- ENSO-induced monsoon change is the primary cause

Correspondence to:
Y. Li,
yuanlong.li@colorado.edu

Citation:
Li, Y., W. Han, J. L. Wilkin, W. G. Zhang, H. Arango, J. Zavala-Garay, J. Levin, and F. S. Castruccio (2014), Interannual variability of the surface summertime eastward jet in the South China Sea, *J. Geophys. Res. Oceans*, *119*, 7205–7228, doi:10.1002/2014JC010206.

Received 2 JUN 2014
Accepted 2 OCT 2014
Accepted article online 6 OCT 2014
Published online 27 OCT 2014

Abstract The summertime eastward jet (SEJ) located around 12°N, 110°E–113°E, as the offshore extension of the Vietnam coastal current, is an important feature of the South China Sea (SCS) surface circulation in boreal summer. Analysis of satellite-derived sea level and sea surface wind data during 1992–2012 reveals pronounced interannual variations in its surface strength (S_{SEJ}) and latitudinal position (Y_{SEJ}). In most of these years, the JAS (July, August, and September)-mean S_{SEJ} fluctuates between 0.17 and 0.55 m s^{-1}, while Y_{SEJ} shifts between 10.7°N and 14.3°N. These variations of the SEJ are predominantly contributed from the geostrophic current component that is linked to a meridional dipole pattern of sea level variations. This sea level dipole pattern is primarily induced by local wind changes within the SCS associated with the El Niño-Southern Oscillation (ENSO). Enhanced (weakened) southwest monsoon at the developing (decaying) stage of an El Niño event causes a stronger (weaker) SEJ located south (north) of its mean position. Remote wind forcing from the tropical Pacific can also affect the sea level in the SCS via energy transmission through the Philippine archipelago, but its effect on the SEJ is small. The impact of the oceanic internal variability, such as eddy-current interaction, is assessed using an ocean general circulation model (OGCM). Such impact can lead to considerable year-to-year changes of sea level and the SEJ, equivalent to ~20% of the observed variation. This implies the complexity and prediction difficulty of the upper ocean circulation in this region.

1. Introduction

The South China Sea (SCS) is a marginal sea of the western tropical Pacific Ocean, covering a large area between 3°S and 23°N with an average basin depth of over 2000 m. It is bounded by the Asian continent and multitude islands and connected with the western Pacific and other marginal seas through narrow straits [e.g., *Wyrtki*, 1961; *Shaw*, 1991; *Han et al*., 2009; *Sprintall et al*., 2012]. Under the influence of the East Asian monsoonal winds, the basin-scale upper ocean circulation has an evident seasonality, exhibiting a cyclonic pattern in boreal winter (boreal omitted hereafter) and an anticyclonic pattern in summer [e.g., *Chu et al*., 1999; *Qu*, 2000; *Liu et al*., 2001; *Fang et al*., 2002; *Gan et al*., 2006]. Recent studies suggest that the SCS circulation is potentially important for the heat exchange between the tropical Pacific and Indian oceans and the regional climate [e.g., *Qu et al*., 2005, 2006, 2009; *Fang et al*., 2009; *Du and Qu*, 2010].

The prevailing southwest monsoon in summer induces coastal upwelling and drives a northeastward flowing coastal current along the Vietnamese coast (Figure 1). The cold sea surface temperature (SST), produced by coastal upwelling, extends eastward into the SCS interior [*Shaw and Chao*, 1994; *Kuo et al*., 2000; *Qu*, 2001; *Dippner et al*., 2007; *Hai et al*., 2010]. This cold water extension is referred to as the "cold filament" by *Xie et al*. [2003]. Its mean temperature is usually 1–2°C lower than the surrounding water. The cold filament has a large impact on the basinwide SST, which decreases from spring to summer in spite of the solar radiation increase. The SST in the mid-SCS basin reaches a minimum after the onset of the southwest summer monsoon (July–September in Figure 1), giving rise to the evident semiannual cycle of the basin-average SST [*Xie et al*., 2003, 2007].

The regional circulation off the Vietnam coast is complicated and highly variable. The northeastward flowing Vietnam coastal current separates from the coast and feeds an eastward flowing jet [*Liu et al*., 2001]. This summertime eastward jet (SEJ), which is also manifested by the large sea surface height (SSH) gradients

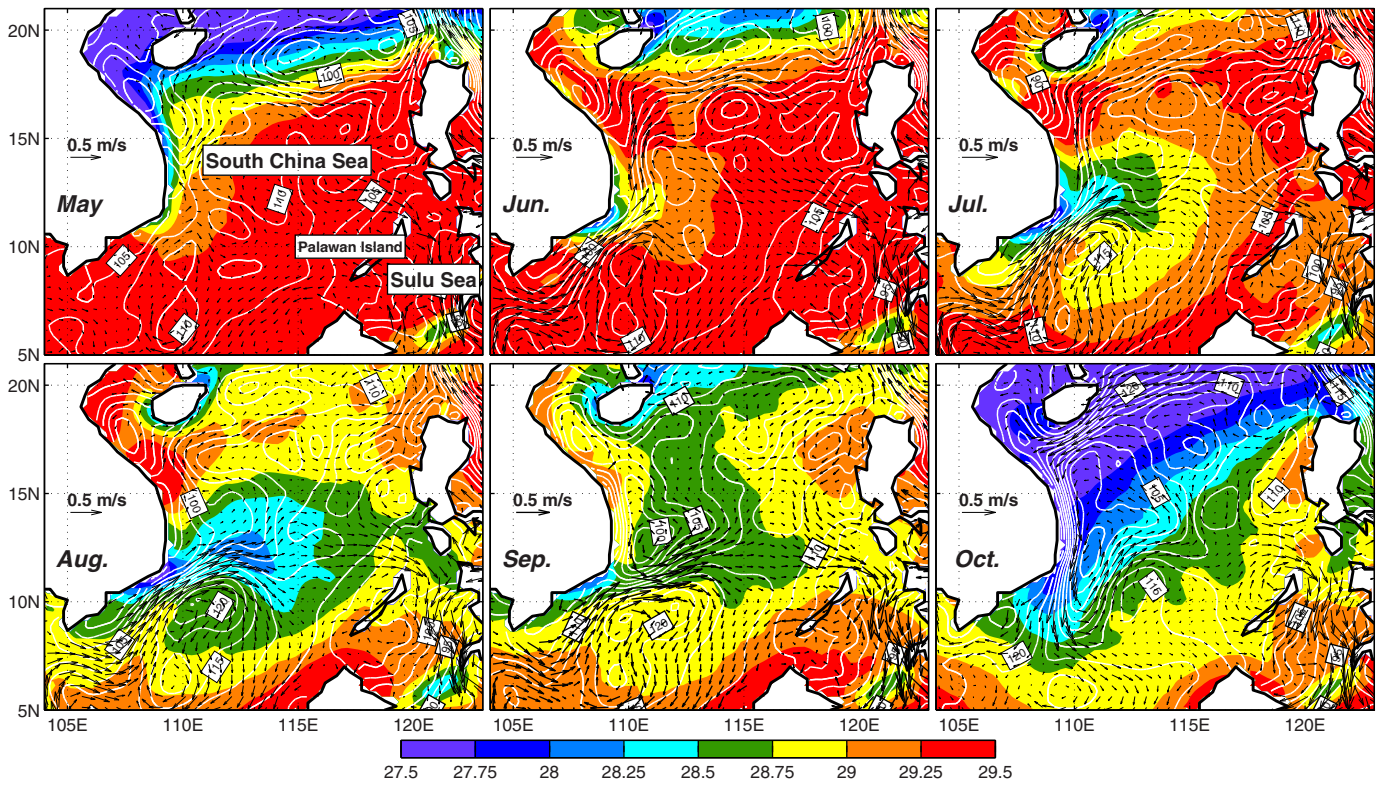

Figure 1. Monthly climatology of SST (color shading; in °C), surface current (vectors; in m s^{-1}), and SSH (white contours; in cm) for May–October during October 1992 through December 2012, based on, respectively, the NOAA optimum interpolated (OI) SST [*Reynolds et al*., 2007], the Ocean Surface Current Analyzes-Real time (OSCAR) product [*Bonjean and Lagerloef*, 2002], and the Archiving, Validation, and Interpretation of Satellite Oceanographic data (AVISO) sea level data [*Le Traon et al*., 1998; *Ducet et al*., 2000].

between 110°E and 113°E during July, August, and September (JAS; Figure 1), transports the cold water from the upwelling zone into the interior SCS basin. The SEJ bounds two circulation gyres, with a cyclonic gyre to its north and an anticyclonic gyre to its south [e.g., *Metzger and Hurlburt*, 1996; *Wu et al*., 1999; *Wang et al*., 2003]. The anticyclonic gyre is larger in size with its high-SSH center at 9°N–10°N, while the cyclonic gyre is smaller with its low-SSH center near 13°N. This double-gyre structure is also termed as the summertime dipole [*G. Wang et al*., 2006] or the eddy pair [*Chen et al*., 2011] in existing literature. Such circulation pattern is conducive to the development of the cold filament, and its variation is hence an important factor modulating the basin-scale SST and regional climate variability. Besides, circulation variations off the Vietnam coast also affect the nutrient distribution and biomass productivity in the SCS [e.g., *Tang et al*., 2004; *Bombar et al*., 2010; *Liu et al*., 2012; *Chen et al*., 2014].

Modeling studies are carried out recently to explore the dynamics of the upper ocean circulation off the Vietnam coast. *Gan and Qu* [2008] suggested that wind stress forcing, nonlinear advection, and the shallow slope topography are important for the separation of the Vietnam coastal current. On the other hand, *Chen et al*. [2012] showed that buoyancy forcing by river discharge and stratified tidal rectification can result in the costal current separation without wind forcing. Using a reduced gravity model, *G. Wang et al*. [2006] investigated the dynamics of the double gyre. They demonstrated that vorticity transport by nonlinear advection is crucial for the formation of the double-gyre structure, and local wind forcing plays a significant role in determining its variability. By analyzing ocean reanalysis data, *Wang et al*. [2010] identified pronounced decadal variations of the SEJ and the double gyre. They shifted southward from 1960 to 1979, northward during 1980–1998, and southward again since 1998, which are primarily induced by the decadal changes of the SCS summer monsoon.

Despite the above findings, our knowledge about the dynamics of the SEJ is far from complete. While large year-to-year variations in SCS sea level, SST, and upper ocean circulation have been reported and shown to be highly correlated with the El Niño-Southern Oscillation (ENSO) indices [e.g., *Chao et al*., 1996; *Xie et al*.,

2003; *Qu et al.*, 2004; *Fang et al.*, 2006; *C. Wang et al.*, 2006; *Rong et al.*, 2007; *Chang et al.*, 2008; *Liu et al.*, 2011; *Dippner et al.*, 2013], interannual variability of the SEJ has never been systematically examined. Proceeding of relevant research is hampered by the ability of existing ocean general circulation models (OGCMs) to simulate the key processes associated with the SEJ variability. On the other hand, accumulation of the high-quality sea level and sea surface wind data from satellite measurements over the past two decades has provided us a powerful tool to monitor and understand the variability of ocean currents. Analyzing satellite data can provide useful insights into the complicated upper ocean processes in this region. The knowledge can be great impetus for the development of the model simulation and data assimilation. In this study, we attempt to characterize and explain the SEJ interannual variability through analyzing satellite data and performing model experiments.

The remainder of the paper is organized as follows. Section 2 gives a brief description of the data, methods, and models utilized in this study. Section 3 characterizes the interannual variations of the surface SEJ based on satellite-derived sea level and wind data. Section 4 explores the wind forcing, ocean responses, and ENSO effects associated with the SEJ variability. In section 5, we provide some discussion concerning the unique case in 2010 and the possible effect of ocean internal variability. Section 6 summarizes the main findings of the paper.

2. Data and Model

2.1. Data

To characterize the surface wind forcing imposed on the ocean, we use 0.25° × 0.25° Cross-Calibrated Multiplatform (CCMP) ocean 10 m wind vectors [*Atlas et al.*, 2008] during October 1992–December 2011. Zonal and meridional surface wind stress, τ_x and τ_y, are calculated from the CCMP 10 m wind speed $|W_{10}|$ using the standard bulk formula

$$\tau_x = \rho_a c_d |W_{10}| u_{10}, \tau_y = \rho_a c_d |W_{10}| v_{10}, \quad (1)$$

where $\rho_a = 1.175$ kg m^{-3} is the air density, $c_d = 0.0015$ is the drag coefficient, and u_{10} and v_{10} are the zonal and meridional 10 m wind components. The mean JAS wind stress from CCMP features prevailing southwest monsoon (Figure 2a). The Ekman pumping velocity is calculated as $w_E = curl(\tau/f)\ \sigma_o^{-1}$, where f is the Coriolis parameter, and $\sigma_o = 1022$ kg m^{-3} is the mean potential density of the surface Ekman layer. The mean JAS w_E exhibits a meridional dipole structure, with positive values (upwelling) centered off the Vietnam coast and negative values (downwelling) distributed in the southern SCS. This dipole pattern of w_E favors the formation of the double-gyre structure in the upper ocean.

The 0.25° × 0.25°, weekly satellite altimeter SSH product from October 1992 through December 2012, is derived from the multisatellite merged Archiving, Validation, and Interpretation of Satellite Oceanographic data (AVISO) [*Le Traon et al.*, 1998; *Ducet et al.*, 2000]. In order to correct the aliasing of tides and barotropic variability, the altimeter data have been updated with a tidal model GOT2000 and barotropic hydrodynamic model MOG2D-G [*Volkov et al.*, 2007; *Dibarboure et al.*, 2008]. The SSH value is the sum of sea level anomaly and mean dynamic topography based on GRACE data, altimetry measurements, and in situ observations [*Rio et al.*, 2011]. The surface geostrophic velocities are estimated using horizontal gradients of SSH

$$(U_G, V_G) = \frac{g}{f}\left(-\frac{\partial SSH}{\partial y}, \frac{\partial SSH}{\partial x}\right), \quad (2)$$

where g is the gravitational acceleration. During JAS, the most striking feature of the mean SCS surface geostrophic circulation is the separation of the Vietnam coastal current and the formation of the SEJ (Figure 2b). The SEJ has a maximum eastward geostrophic velocity exceeding 0.4 m s^{-1} near 11°N–12°N (Figure 2c).

At the sea surface Ekman flow could be comparable with the geostrophic flow under strong wind condition. The surface Ekman current in the northern hemisphere is 45° to the right of the wind direction [*Ekman*, 1905] (although there has been studies showing that the angle could be smaller when more realistic viscosity profile is used [e.g., *Madsen*, 1977]),

$$(U_E, V_E) = V_0[\cos(\pi/4),\ \sin(\pi/4)], \quad (3)$$

where $V_0 = 0.0068|W_{10}|(\sin\varphi)^{-1/2}$ is the magnitude of the surface Ekman current [*Ralph and Niiler*, 1999]. Compared to the 0.4 m s^{-1} surface geostrophic current, surface Ekman drift contributes to ~20% of the

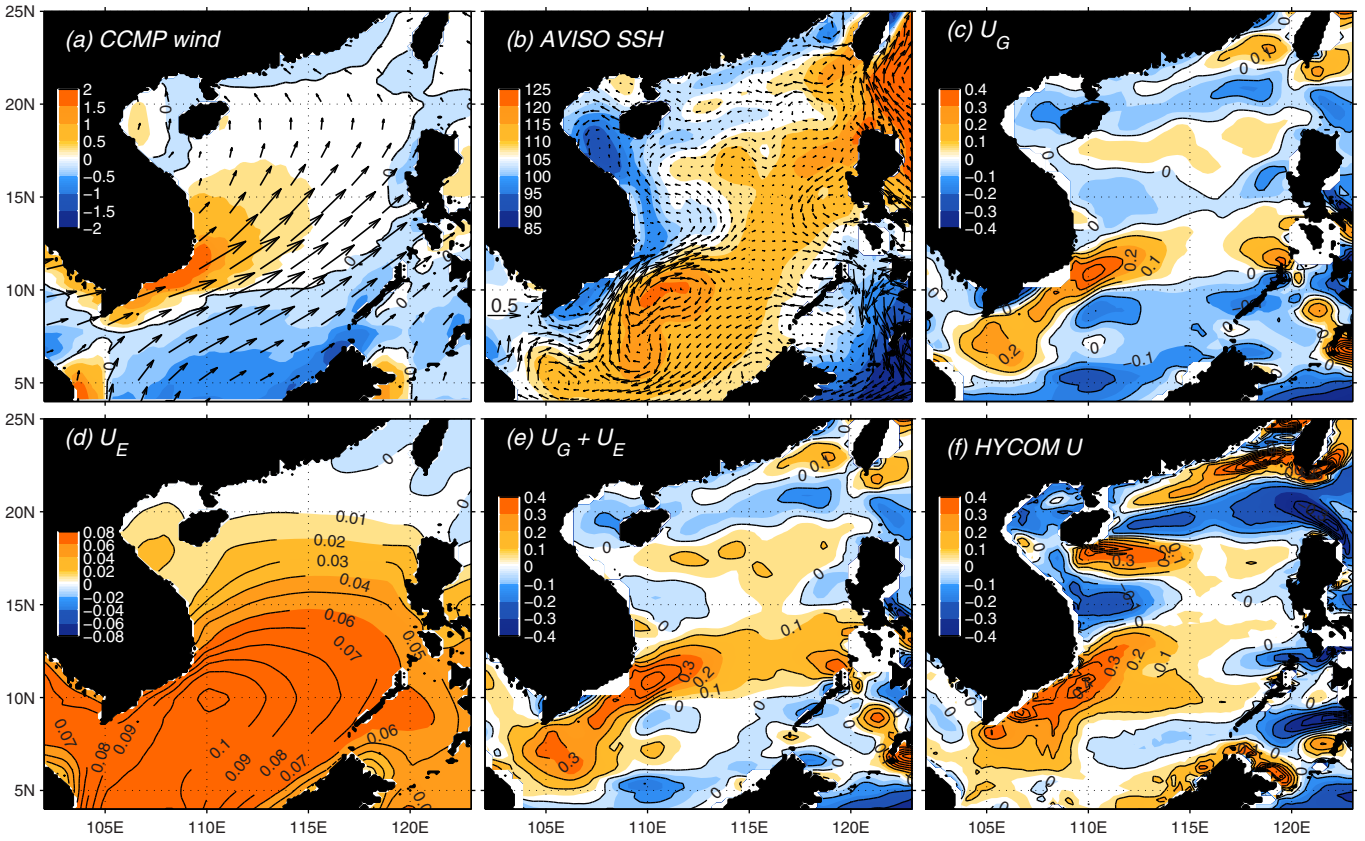

Figure 2. Climatologic JAS (July, August, and September)-mean maps of (a) wind stress (vectors; in N m^{-2}) and Ekman pumping velocity w_E (color shading; in 10^{-5} m s^{-1}), (b) SSH (color shading; in cm) and surface geostrophic current (vectors; in m s^{-1}), (c) zonal surface geostrophic current U_G (m s^{-1}), (d) zonal surface Ekman flow U_E, and (e) the total zonal surface current $U = U_G + U_E$. Here SSH and geostrophic current are based on AVISO sea level product during 1992–2012, while wind stress, w_E, and U_E are calculated with CCMP wind data during 1992–2011. (f) Climatologic JAS-mean zonal surface current U from HYCOM control run during 2006–2011.

mean SEJ. In this study, we will use the total surface current, $U = U_E + U_G$ (Figure 2e), to assess the SEJ variability, instead of using the Ocean Surface Current Analyzes-Real time (OSCAR) product [*Bonjean and Lagerloef*, 2002]. This is because the OSCAR data have no records in areas close to the coast for a long period of time, which brings difficulties in extracting continuous time series of the SEJ-related parameters for the entire data period of 1992–2012. During periods with good data coverage, OSCAR zonal currents are consistent with our estimated total surface U. Note that the estimated U here does not contain nonlinear part of the oceanic current, which is discussed in section 5.2.

We also use the 1/4° × 1/4° optimum interpolated (OI) SST product [*Reynolds et al.*, 2007] from the National Oceanic and Atmospheric Administration (NOAA), which is based on the Advanced Very High Resolution Radiometer (AVHRR) infrared satellite SST and Advanced Microwave Scanning Radiometer (AMSR) SST data. To examine the impact from ENSO, the Niño-3.4 index is taken from the Climate Prediction Center of NOAA as a proxy of ENSO variability.

To address interannual variations, we analyze two types of anomaly. In this study, anomaly of a variable refers to the temporal deviation from its climatological mean value. The first is yearly JAS-mean anomaly, since the SEJ is fully developed during the 3 months (Figure 1). The second is low-passed monthly anomaly, for which climatological seasonal cycle and the linear trend are removed and a 13 month Hanning filter is applied to damp higher-frequency signals.

2.2. Model

The OGCM used in this study is the HYbrid Coordinate Ocean Model (HYCOM) version 2.2.18 [*Wallcraft et al.*, 2009]. It is configured to the Indo-Pacific basin (30°E–70°W, 40°S–40°N) with a horizontal resolution of 0.25° × 0.25° [*Li et al.*, 2013]. The model has 35 vertical layers with 10 layers in the top 11 m to better resolve

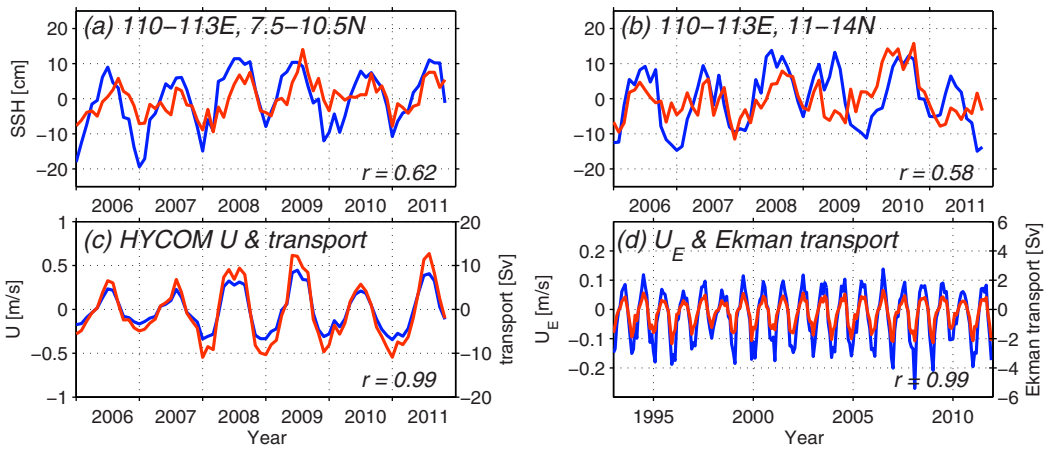

Figure 3. (a) Monthly SSHA (cm) averaged over the area 110°E–113°E, 7.5°N–10.5°N from the HYCOM control run (blue) and AVISO sea level product (red). Figure 3b is the same as Figure 3a except the area 110°E–113°E, 11°N–14°N. (c) Simulated surface U (blue; m s^{-1}) averaged over 110°E–113°E, 9°N–14°N and zonal current transport above 150 m (red; in Sv) between 9°N and 14°N averaged over 110°E–113°E from HYCOM control run. (d) Surface U_E (blue; m s^{-1}) averaged over 110°E–113°E, 9°N–14°N and zonal Ekman transport (red; in Sv) between 9°N and 14°N averaged over 110°E–113°E computed with CCMP wind data.

near-surface ocean processes. The surface atmospheric forcing fields include surface short-wave and long-wave radiations from the Clouds and the Earth's Radiant Energy System (CERES) [*Wielicki et al.*, 1996], precipitation from the Tropical Rainfall Measuring Mission (TRMM) Multisatellite Precipitation Analysis (TMPA) product [*Kummerow et al.*, 1998], CCMP winds, and 2 m air temperature and humidity from the European Centre for Medium-Range Weather Forecasts (ECMWF) Re-analysis Interim (ERA-Interim) product [*Dee et al.*, 2011]. The model is spun-up from a state of rest with monthly climatologic forcing for 35 years (climatologic run), and then integrated forward with daily forcing from January 2005 to November 2011 (control run).

The simulated mean SEJ has a maximal U of 0.4–0.5 m s^{-1} at around 11°N–12°N (Figure 2f), which is close to the observed SEJ. The major model-data discrepancy occurs in the northern SCS, where the Kuroshio intrusion through the Luzon Strait is much stronger. A strong anticyclonic recirculation gyre occurs between 15°N and 18°N, which is also likely related to the overlarge Kuroshio loop in the model. These discrepancies however have limited influence on the SEJ area. The simulated SSH variations are quite consistent with observation (Figures 3a and 3b), with very close amplitudes and linear correlations of 0.62 and 0.58 in two selected areas, which will be shown important for the SEJ variability. Besides the imperfection of the model, the inconsistent part of the variance may also arise from the nonlinear ocean variability, which is basically unpredictable for OGCMs.

The model result can help us to check whether the surface current is a good representative of surface-layer transport. Within the mean SEJ area of 110°E–113°E, 7.5°N–10.5°N, monthly surface U is highly correlated with the zonal transport integrated in the top 150 m ($r = 0.99$; Figure 3c). On the other hand, surface U_E correlates with zonal Ekman transport with also $r = 0.99$ (Figure 3d). Such comparison suggests the reasonability of using the satellite-based surface U_G and U_E as proxies of surface-layer geostrophic and Ekman currents. We can also see that a 0.1 m s^{-1} change of surface U corresponds roughly to a 3 Sv (1 Sv = 10^6 m^3 s^{-1}) change in zonal transport, while a 0.1 m s^{-1} change of surface U_E corresponds to only a 1.0–1.5 Sv change of Ekman transport. Therefore, our investigation using observed surface U_E will not underestimate the contribution of Ekman flow in the SEJ variability.

Besides the HYCOM, outputs from several other eddy-resolving OGCMs are also analyzed. They are the 0.1° eddy-resolving OGCM for the Earth Simulator (OFES) [*Masumoto et al.*, 2004], a 7 km Regional Ocean Modeling System (ROMS) configured for the SCS, and a 5 km ROMS configured for the Coral Triangle (CT) region (CT-ROMS; 95°E–170°E, 25°S–25°N) [*Castruccio et al.*, 2013]. The two ROMS simulations include river discharge and tidal forcing.

3. Observed Interannual Variations of the SEJ

The standard deviation (STD) of the yearly JAS-mean U_G measures the overall interannual variability of summertime geostrophic current for the 1993–2012 period (Figure 4a). The largest STD values in the SCS occur near the SEJ area, exceeding 0.15 m s^{-1} between 9°N and 15°N and reaches a maximum of >0.2 m s^{-1}

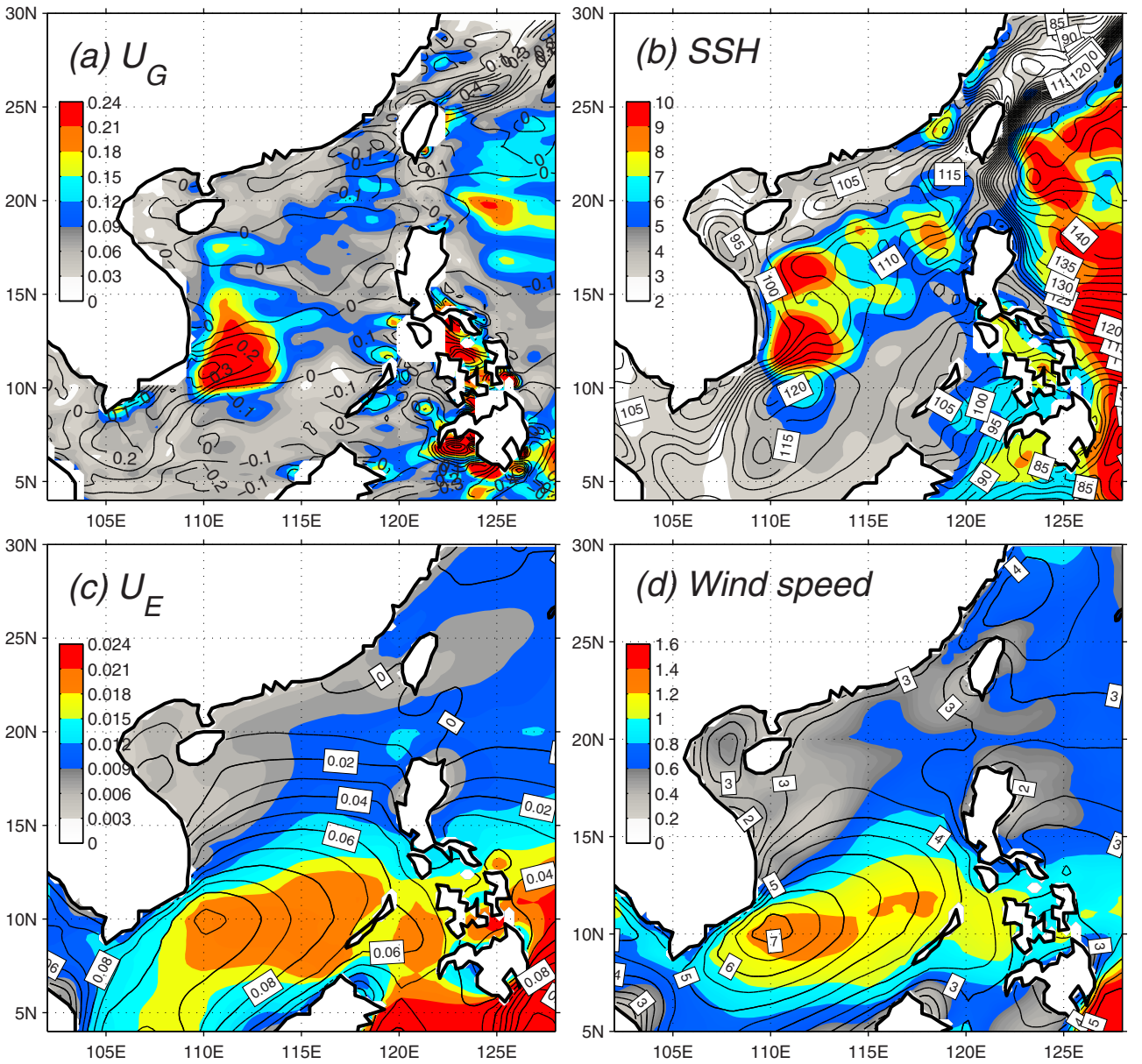

Figure 4. Standard deviation (STD) of the yearly JAS-mean zonal geostrophic current U_G (m s^{-1}), (b) SSH (cm), (c) U_E (m s^{-1}), and (d) wind speed (m s^{-1}). The climatologic JAS-mean maps of these variables are superimposed as black contours. U_G and SSH are based on AVISO sea level product during 1993–2012, while U_E and wind speed are based on CCMP wind data during 1993–2011.

along the axis of the climatological SEJ. This area is also of strong SSH variability (Figure 4b), with STD values exceeding 9 cm. Another high STD patch appears between 15°N and 17°N with similar magnitudes, but it induces weaker U_G changes in Figure 4a. This is attributed to higher latitude (larger *f*) and, more importantly, the spatial structure of SSH variations. We will show in section 4 that SSH variations near the SEJ are characterized by out-of-phase anomalies on the two sides of the SEJ, which give rise to larger change of SSH gradient at the SEJ and hence larger U_G variation. SSH variations at 15°N–17°N are also relatively distant from the SEJ and likely have little impact on the SEJ variability. The distribution of surface Ekman current variability (Figure 4c) generally follows that of wind speed (Figure 4d), with large STDs concentrated around the strong wind jet between 7°N and 12°N. In comparison with geostrophic current, the Ekman current has much weaker interannual variability. The STD of U_E is between 0.01 and 0.02 m s^{-1}, which is one order smaller than that of U_G. These maps tell us that the SEJ has the strongest interannual variability in the summertime SCS circulation, which is dominated by geostrophic current variability.

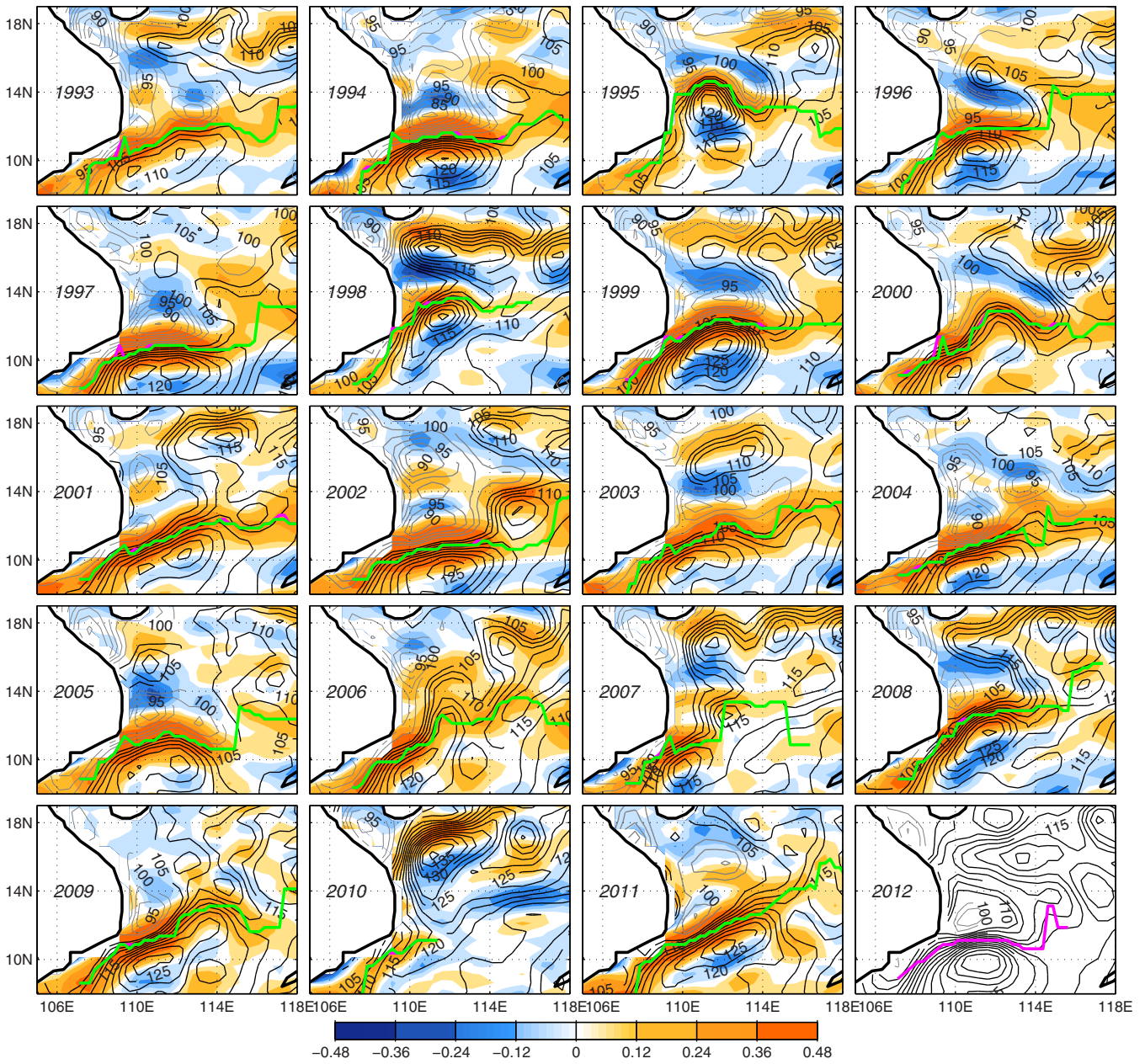

Figure 5. Yearly JAS-mean maps of zonal surface current U (color shading; in m s^{-1}) and SSH (black contours; in cm) during 1993–2012. The green curve denotes the axis of the SEJ (Y_{SEJ}; see the text for the definition), while the pink curve represents the axis determined by only geostrophic current (Y_G). SSH values larger (smaller) than 105 cm are shown by black (gray) contours. In the 2012 map, only SSH and Y_G are shown due to the unavailability of CCMP wind data.

To reveal the year-to-year evolution of the SEJ, we display the yearly images of JAS-mean U and SSH during 1993–2012 in Figure 5. To track the SEJ path, we define the axis of the SEJ as the meridional maximum of eastward U between 8°N and 16°N with a magnitude exceeding 0.1 m s^{-1} (green curves; denoted by Y_{SEJ}). Among the 19 summers of 1993–2011, 18 SEJs can be traced to at least 116°E. The only exception occurs in 2010, when no organized SEJ can be identified in this region. We denote the 2010 case as a disappearance case. The SEJ exhibits evident interannual variability. In some years, such as 1994, 1997, and 2002, the SEJ is strong and has a west-east path around 11°N, with a maximum U_G of >0.4 m s^{-1}. In most other years, the SEJ tilts northeastward with smaller velocities. Interestingly, in 1995 and 1998, the entire SEJ is displaced northward to 13°N–15°N. The Vietnam coastal current does not leave the coast at its mean latitude of 11°N–12°N. Instead, it continues flowing northward along the Vietnam coast until 13°N or above before separating the coast to feed the SEJ.

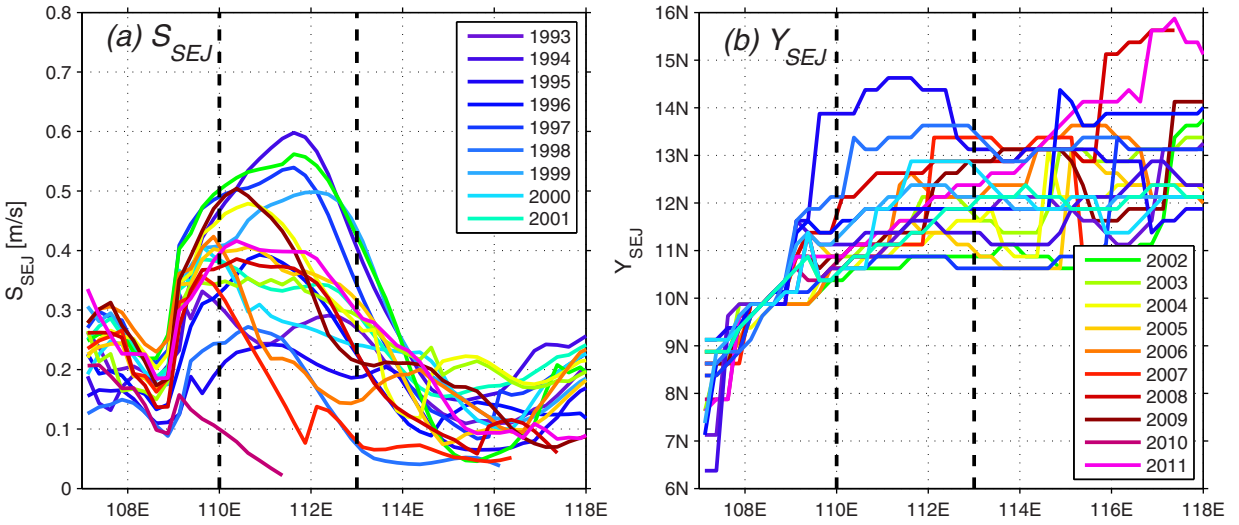

Figure 6. (a) The JAS-mean surface strength S_{SEJ} (m s^{-1}) and (b) axis position Y_{SEJ} (°N) of the SEJ as functions of longitude. Different colors denote different years of 1993–2011. Longitudes of 110°E−113°E are remarked with two dashed lines.

The SEJ variability in its strength and location is closely associated with SSH changes in the double-gyre area. For example, the southward shifted, strong SEJs in 1994, 1997, and 2002 are accompanied by large, strong double-gyre structures. For such cases, the cyclonic gyre (SSH < 105 cm) revolves around 111°E, 12°N, and the anticyclonic gyre is located further south. In contrast, the northward shifted, weak SEJs in 1995 and 1998 are accompanied by northward shifted, weak double-gyre structures, with a high (rather than low) SSH center (> 115 cm) located around 111°E, 12°N. In each plot, Y_{SEJ} always occurs at the maximal meridional SSH gradient (∂SSH/∂y), which is also the boundary between the two gyres. The SEJ axis computed with only U_G (Y_G; pink curves in Figure 5) basically overlaps with Y_{SEJ}. These results further demonstrate the dominance of geostrophic current in determining the location and strength of the surface SEJ. Note that there is an eastward flow at ~17°N in the northern SCS. This flow can be very strong in some years such as 1998, 1999, 2007, 2008, and 2010. This eastward current is not directly related to the SEJ but appears to be associated with the anticyclonic recirculation gyre centered between 15° and 17°N, which also exhibits large interannual SSH variability.

To quantify the variability of the SEJ, we calculate the JAS-mean surface strength (S_{SEJ}) and axis position (Y_{SEJ}) as functions of longitude (Figure 6). Here S_{SEJ} is computed by averaging eastward U ($U > 0$) within a 3° latitude band centered at Y_{SEJ},

$$S_{SEJ}(x,t) = \frac{\int_{Y_{SEJ}-1.5^o}^{Y_{SEJ}+1.5^o} U(x,y,t)dy}{L_y}, \quad (4)$$

where L_y is the meridional distance between $Y_{SEJ} - 1.5°$ and $Y_{SEJ} + 1.5°$. In most years, the SEJ obtains its maximal strength and organized jet-like structure between 110°E and 113°E (Figure 6a). There are also large year-to-year variations within this longitude range. The S_{SEJ} varies between 0.17 and 0.55 m s^{-1}, except for the 2010 disappearance case with S_{SEJ} value smaller than 0.1 m s^{-1} west of 111.5°E. Meanwhile, the Y_{SEJ} shifts between 10.7°N and 14.3°N at these longitudes (Figure 6b). In fact, most SEJs locate between 10.7°N and 12.9°N, while only the 1995 and 1998 cases have Y_{SEJ} shifted to north of 13°N. Fluctuation of Y_{SEJ} is also strong east of 113°E, but S_{SEJ} drops quickly as proceeding eastward and gradually gets diffused. At 114°E S_{SEJ} has been <0.2 m s^{-1}. Current west of 110°E has not completely separated from the coast yet, and the SEJ has not been fully developed. Therefore, hereafter we will focus on the variations within 110°E–113°E where the main jet body falls.

4. Wind Forcing and Ocean Response

4.1. Wind Forcing

Given the importance of wind forcing, it is instructive to examine the wind variations in the SCS and its relationship with the SEJ variability. In Figure 7 we display the year-to-year changes of surface wind stress

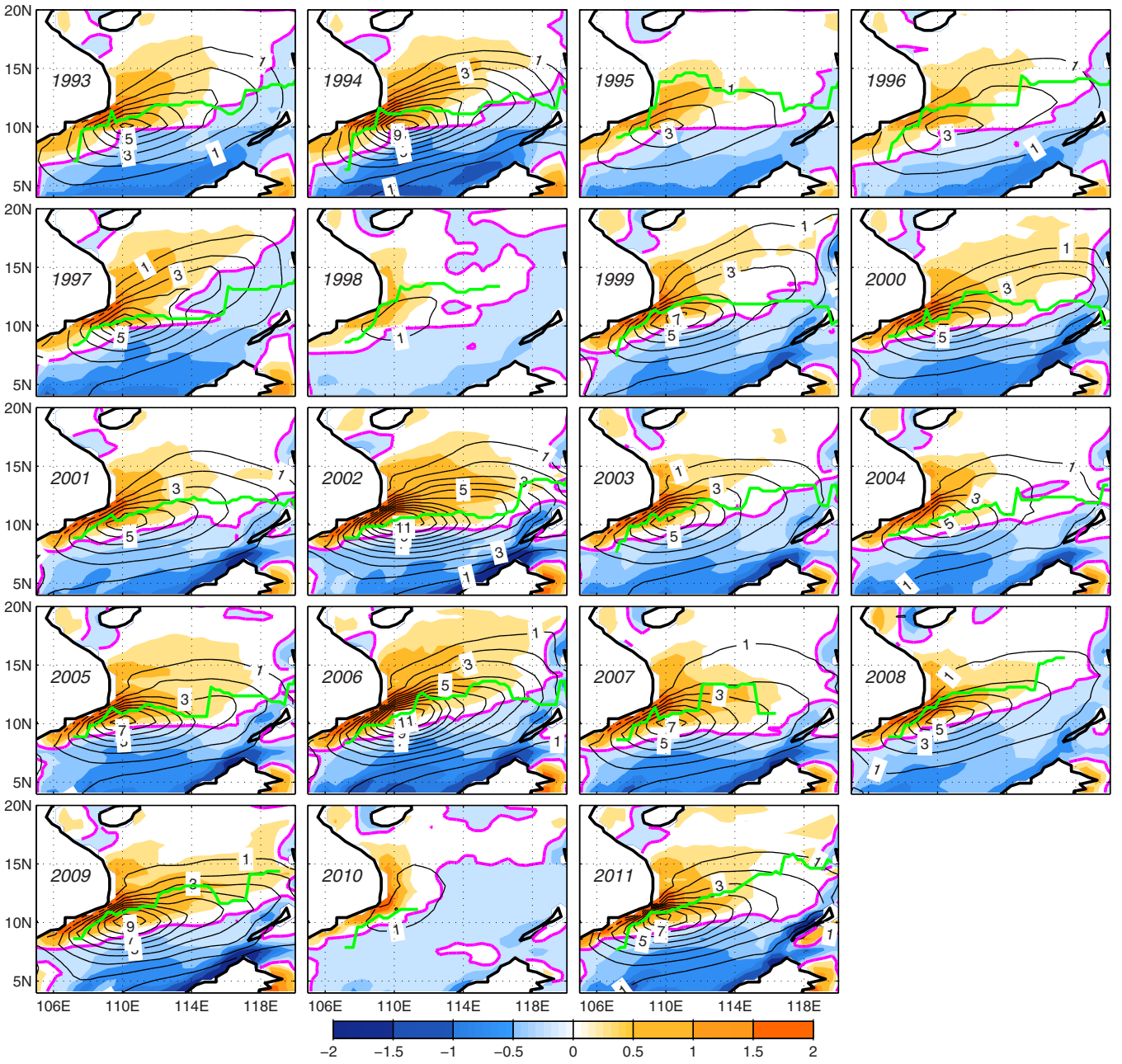

Figure 7. Yearly JAS-mean maps of Ekman pumping velocity w_E (color shading; in 10^{-5} m s^{-1}) and wind stress (black contours; in 10^{-2} N m^{-2}) for the years 1993–2011. The green curve denotes Y_{SEJ}, while the pink curve represents the zero w_E contour.

magnitude and Ekman pumping velocity w_E. The latter is the primary driver for the low-frequency SSH and upper ocean geostrophic current variations in the tropics [e.g., *Meyers*, 1979; *Kessler*, 1990; *Chelton and Schlax*, 1996]. Off the Vietnam coast where the southwest monsoon attains its maximal strength, wind stress magnitude varies widely between 0.01 and 0.12 N m^{-2}. During 1995, 1998, and 2010 when the SEJ shifts north of 13°N or simply disappears, winds are anomalously weak compared to other years. Correspondingly, the positive/negative meridional dipole pattern of w_E is evidently weaker than normal. By contrast, during 1994, 1997, and 2002 when the SEJ is strong and shifted south, wind stress and w_E dipole are stronger than normal.

To further understand the SEJ-wind relationship, we plot out the time series of JAS-mean S_{SEJ} and wind stress magnitude in Figure 8a. Here we computed two versions of the wind stress: the basin-averaged wind stress in the SCS (blue curve; 105°E–120°E, 4°N–18°N) and the local wind stress in the vicinity of the SEJ

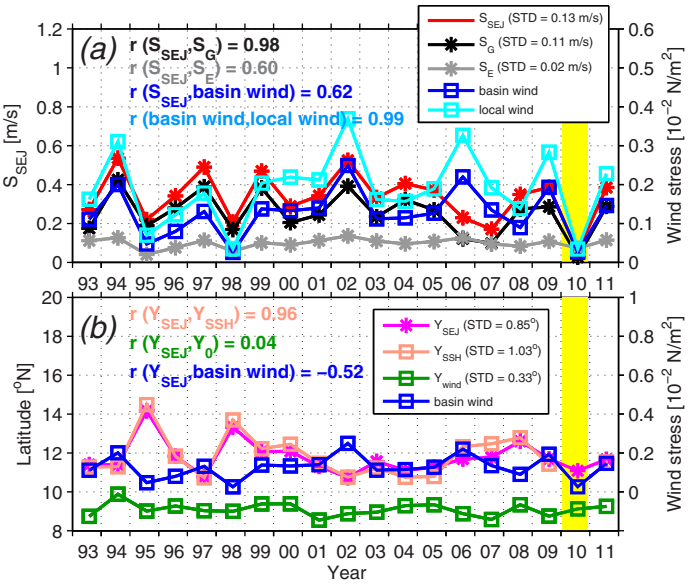

Figure 8. (a) Yearly JAS-mean time series of S_{SEJ} (m s^{-1}), its geostrophic component S_G, Ekman component S_E averaged between 110°E and 113°E, SCS basin-averaged wind stress (in 10^{-2} N m^{-2}; 105°E–120°E, 4°N–18°N), and local wind stress southeast of Vietnam coast (in 10^{-2} N m^{-2}; 109°E–114°E, 9°N–14°N). (b) Yearly JAS-mean time series of Y_{SEJ} (°N) averaged between 110°E and 113°E, the mean latitude of the 110 cm SSH contour between 110°E and 113°E (°N), the zero value latitude Y_0 of the zonally integrated w_E over the SCS (°N), and the wind stress averaged over the SCS basin (10^{-2} N m^{-2}). Yellow shading denotes the 2010 disappearance case.

(cyan curve; 109°E–114°E, 9°N–14°N). The local and basinwide winds are strikingly consonant, with a correlation exceeding 0.99. This means that interannual variability of sea surface wind is spatially accordant in the entire SCS basin, reflecting mainly the intensity changes of the summer monsoon. Given that the SEJ variations can be influenced by wind forcing at different longitudes in the SCS basin through westward propagating Rossby wave signals, hereafter we mainly discuss the basin-averaged wind. Evolutions of S_{SEJ} and basin-averaged wind stress are quite consistent, showing a linear correlation of $r = 0.62$ (above 95% significance level). The peaks of S_{SEJ} in 1994, 1997, 1999, 2002, 2009, and 2011 correspond to the wind stress peaks. Interestingly, these peaks of S_{SEJ} and wind stress are followed by troughs in 1995, 1998, 2000, 2003, and 2010, respectively. There are some disagreements during 2006–2008. In 2006, the wind is strong, but S_{SEJ} is weak. Rechecking Figure 5 reveals that the eastward flows in 2006 spread over the mid-SCS rather than concentrate at the SEJ axis. This flow pattern is likely influenced by oceanic internal variability which extracts energy from the mean flow and generates eddies and meanders. In contrast, in 2008 the wind is weak, but the SEJ is strong. The strong SEJ is accompanied with a strong, well-structured double-gyre pattern without strong eddies or meanders (Figure 5). The effect of eddies due to oceanic internal processes will be further discussed in section 5.2. As expected, geostrophic current (STD of S_G is 0.11 m s^{-1}) overwhelms Ekman current S_E (STD of S_E is 0.02 m s^{-1}) in determining the interannual variations of S_{SEJ} (STD = 0.13 m s^{-1}). The linear correlation is 0.98 between S_{SEJ} and S_G but only 0.60 between S_{SEJ} and S_E.

Y_{SEJ} variations closely follow the meridional shifts of the double-gyre structure (Figure 8b). Here we use the 110 cm contour of the detrended SSH as a proxy for the boundary of the two gyres based on the climatologic distribution (Figure 2b). Y_{SEJ} shows a correlation of $r = 0.96$ and close amplitude (0.85° versus 1.03° in STD) with the mean latitude of 110 cm SSH contour (denoted by Y_{SSH}), suggesting the tight bond between the SEJ location and SSH variations in the surrounding area. Because the double-gyre structure is primarily wind-driven, theoretically, the SEJ should follow the zero line of the Ekman pumping velocity or wind stress curl in the SCS basin [e.g., *Wang et al.*, 2010]. We hence further compare the latitude of zero value of zonally integrated w_E (denoted by Y_{wind}) with Y_{SEJ}. The two curves are however not significantly correlated ($r = 0.04$). The mean Y_{SEJ} is about 2°N of Y_{wind}, and its fluctuation is much larger than Y_{wind} (0.85° versus 0.33° in STD). This lack of correlation is also evident in Figure 7 (compare the green and pink curves). Therefore the meridional shifts of the local wind pattern are not likely the primary cause for Y_{SEJ} variability. This result is not surprising, because the Sverdrup balance predicts the location of the depth-integrated currents, while here we focus on the changes of the surface SEJ. Besides the wind forcing in the SCS, the mean location of Y_{SEJ} can be also influenced by remote winds in the Pacific Ocean through eastern boundary forcing of the SCS [e.g., *Liu et al.*, 2011; *Zhuang et al.*, 2013].

Interestingly, instead of Y_{wind}, the basin-averaged wind stress has a much higher correlation with Y_{SEJ} ($r = -0.52$). The weakened winds in 1995, 1998, and 2008 coincide with northward shifts of the SEJ. In 2010

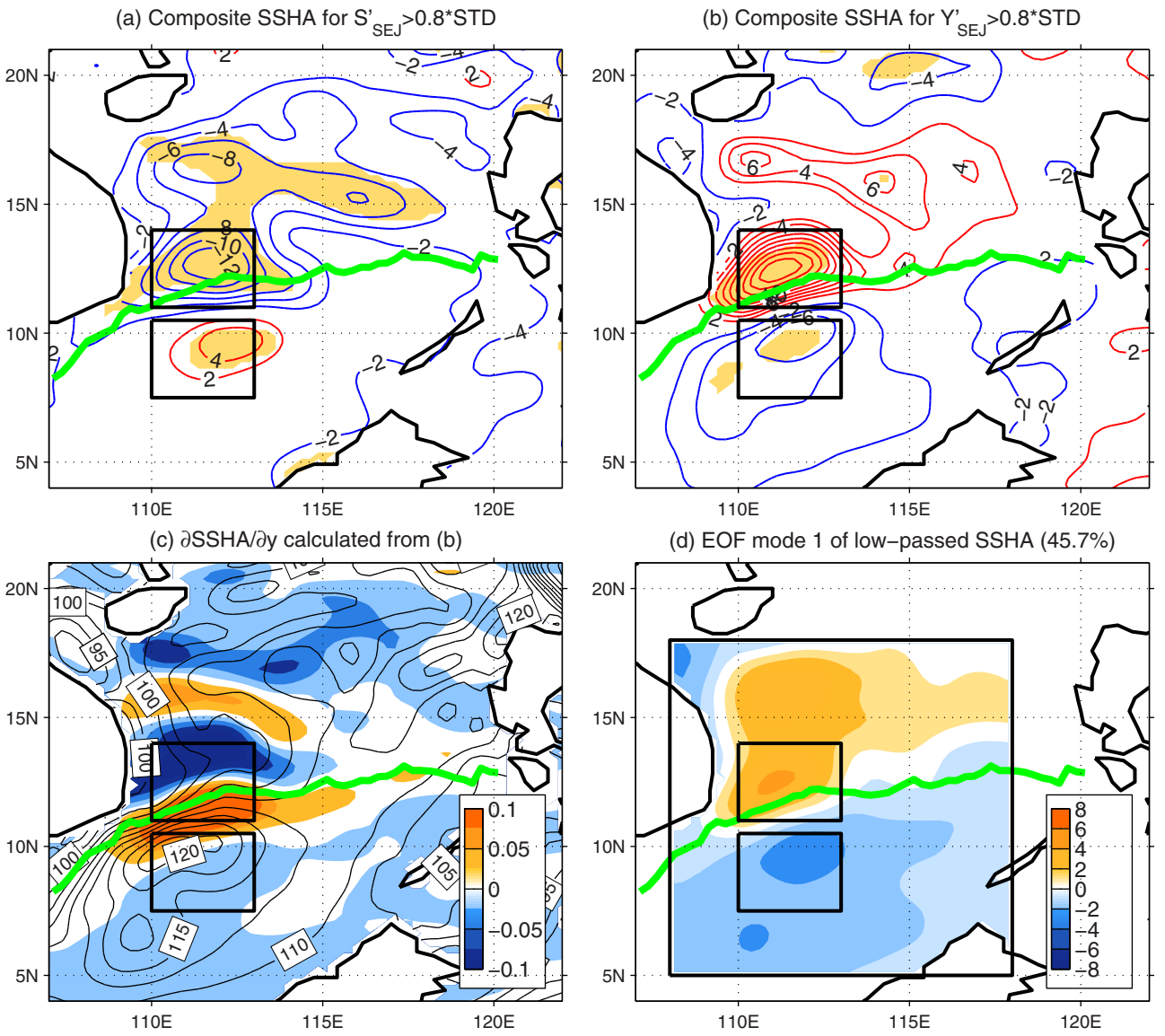

Figure 9. (a) Composite JAS SSHA map for the years with S_{SEJ} anomaly higher than its 0.8 STD value (1994, 1997, 1999, and 2002). (b) Composite JAS-mean SSHA map (cm) for the years with Y_{SEJ} anomaly higher than its 0.8 STD value (1995, 1998, and 2008). The red (blue) contours denote positive (negative) SSHAs, while the yellow shadings highlight SSHAs significant at 90% confidence level based on a two-tailed Student's *t* test. (c) Meridional SSHA gradient $\partial SSHA/\partial y$ (cm km^{-1}) calculated from the composite SSHA in Figure 9b. (d) First EOF mode of 13 month low-passed SSH during JAS, which explains 45.7% of the total variance. The climatological JAS-mean SSH is superimposed as black contours in Figure 9c. The green curve denotes the climatological Y_{SEJ}, while the black rectangles denote the areas of the southern pole (SP; 110°E–113°E, 7.5°N–10.5°N) and northern pole (NP; 110°E–113°E, 11°N–14°N).

disappearance case of the SEJ, the Y_{SEJ} value is meaningless, which leads to the discrepancy between Y_{SEJ} and wind strength. These results suggest that in spite of some exceptional cases, the strength of the southwest monsoon is likely a key factor modulating the interannual variations of S_{SEJ} and Y_{SEJ}. A stronger southwest monsoon leads to a stronger, southward shifted SEJ, while a weaker monsoon results in a weaker, northward shifted SEJ, which leads to a negative correlation between S_{SEJ} and Y_{SEJ} ($r = -0.38$).

4.2. SSH Variations

Since the SEJ variability is related to regional SSH changes via geostrophy, it is necessary to explore the characteristics and driving mechanism of SSH variations. To extract the SSH variations associated with SEJ variability, we compute the composite map of interannual SSH anomaly (SSHA) for years with S_{SEJ} stronger than its 0.8 STD value ($S'_{SEJ} > 0.8 \times$ STD): 1994, 1997, 1999, and 2002. When S_{SEJ} is anomalously large, SSH shows a meridional dipole pattern in the SCS, with positive (negative) SSHAs south (north) of the SEJ (Figure 9a). This SSHA pattern strengthens the double-gyre structure and enhances the eastward geostrophic flow

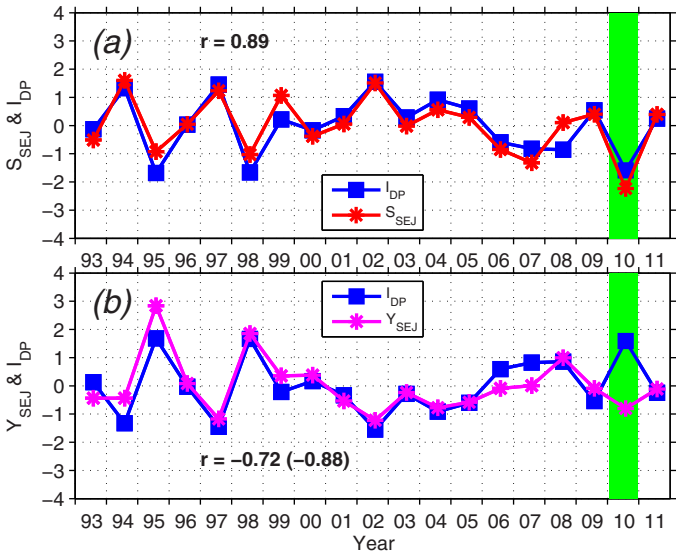

Figure 10. (a) Yearly JAS-mean time series of S_{SEJ} (red) averaged between 110°E and 113°E and the dipole index I_{DP} (blue). (b) Yearly JAS-mean time series of Y_{SEJ} (pink) between 110°E and 113°E and the I_{DP} (blue). To achieve better comparison, all the variables are normalized, and I_{DP} in Figure 10b is multiplied by −1. Green shading denotes the 2010 disappearance case. The correlations between Y_{SEJ} and I_{DP} are −0.72 and −0.88 with and without the 2010 case.

of the SEJ. The composite SSHA for $S'_{SEJ} < -0.8 \times$ STD (involving 5 years) shows a similar significant dipole structure with an opposite sign (not shown). And the composite for the "normal years" ($-0.8 \times$ STD $< S'_{SEJ} < 0.8 \times$ STD) shows no significant SSHA signals in the SCS. The composite SSHA map for $Y'_{SEJ} > 0.8 \times$ STD (Figure 9b) is opposite to Figure 9a, albeit with magnitude differences, while the composite for $Y'_{SEJ} < -0.8 \times$ STD is quite similar to Figure 9a. This indicates that variations of S_{SEJ} and Y_{SEJ} are not independent phenomena but are both associated with a SSHA dipole pattern. The negative phase of the dipole as in Figure 9b, with positive SSHAs in the northern pole and negative SSHAs in the southern pole, can not only weaken the SEJ but also shift it northward; the positive phase of the dipole as in Figure 9a can strength the SEJ and shift it southward. In both Figures 9a and 9b, SSHAs at the two poles are statistically significant at 90% confidence level. We also checked the sensitivity of the results to the choice of criterion. Composite maps using $1.0 \times$ STD and $0.5 \times$ STD criterions show similar patterns (not shown), except that $1.0 \times$ STD includes few samples, while $0.5 \times$ STD degrades the significance.

How can a SSHA pattern in Figure 9b shift Y_{SEJ} northward? This can be elaborated by the meridional SSHA gradient ∂SSHA/∂y map (Figure 9c) calculated from the composite SSHA of Figure 9b, because Y_{SEJ} always occurs at the negative peak of ∂SSH/∂y (Figure 5). The SSHA dipole pattern in Figure 9b results in positive ∂SSHA/∂y anomalies south of the mean SEJ and negative ∂SSHA/∂y anomalies north of it. Therefore, the negative mean ∂SSH/∂y in this region is enhanced in the north and reduced in the south, which leads to the northward shifts of the negative ∂SSH/∂y peak and thus Y_{SEJ}. Similarly, we can expect a southward shift of Y_{SEJ} by the SSHA pattern in Figure 9a. The SSHA dipole is captured by the leading mode of empirical orthogonal function (EOF) analysis of the 13 month low-passed SSHA in the area of 108°E–118°E, 5°N–18°N during JAS months (Figure 9d), explaining 45.7% of the total variance. The result indicates that the SSHA dipole, which modulates both S_{SEJ} and Y_{SEJ} variations, accounts for a large portion of the interannual SSH variability in the SCS. It is important to note that the location of this SSHA dipole does not geographically coincide with the mean double gyre. The mean SEJ, as the climatological boundary of the two gyres, is located within the northern pole of SSHA (the northern rectangle in Figure 9).

Given the importance of this SSHA dipole pattern, we define a dipole index I_{DP} as the JAS-mean SSHA difference between the southern pole (SP; 110°E–113°E, 7.5°N–10.5°N) and the northern pole (NP; 110°E–113°E, 11°N–14°N), $I_{DP} = SSHA_{SP} - SSHA_{NP}$. Interannual changes of this dipole index are fairly consistent with those of S_{SEJ} and Y_{SEJ}, with correlation coefficients of 0.89 (>99% significance) and −0.72 (>95% significance) with S_{SEJ} and Y_{SEJ}, respectively (Figure 10). Its correlation with Y_{SEJ} is degraded by the 2010 disappearance case. Excluding the 2010 Y_{SEJ} value raises the correlation to −0.88 (>99% significance). These comparisons suggest that I_{DP} is a good proxy in representing the variability of the SEJ regarding both S_{SEJ} and Y_{SEJ}.

Below, we examine how the wind forcing affects the variations of I_{DP}. At the latitudes of the SP (7.5°N–10.5°N), longitude-time plot of the SSHA shows westward propagation across the SCS (Figure 11a). It takes several months for SSHAs to travel from the eastern boundary (in fact within the Sulu Sea) to the SP region.

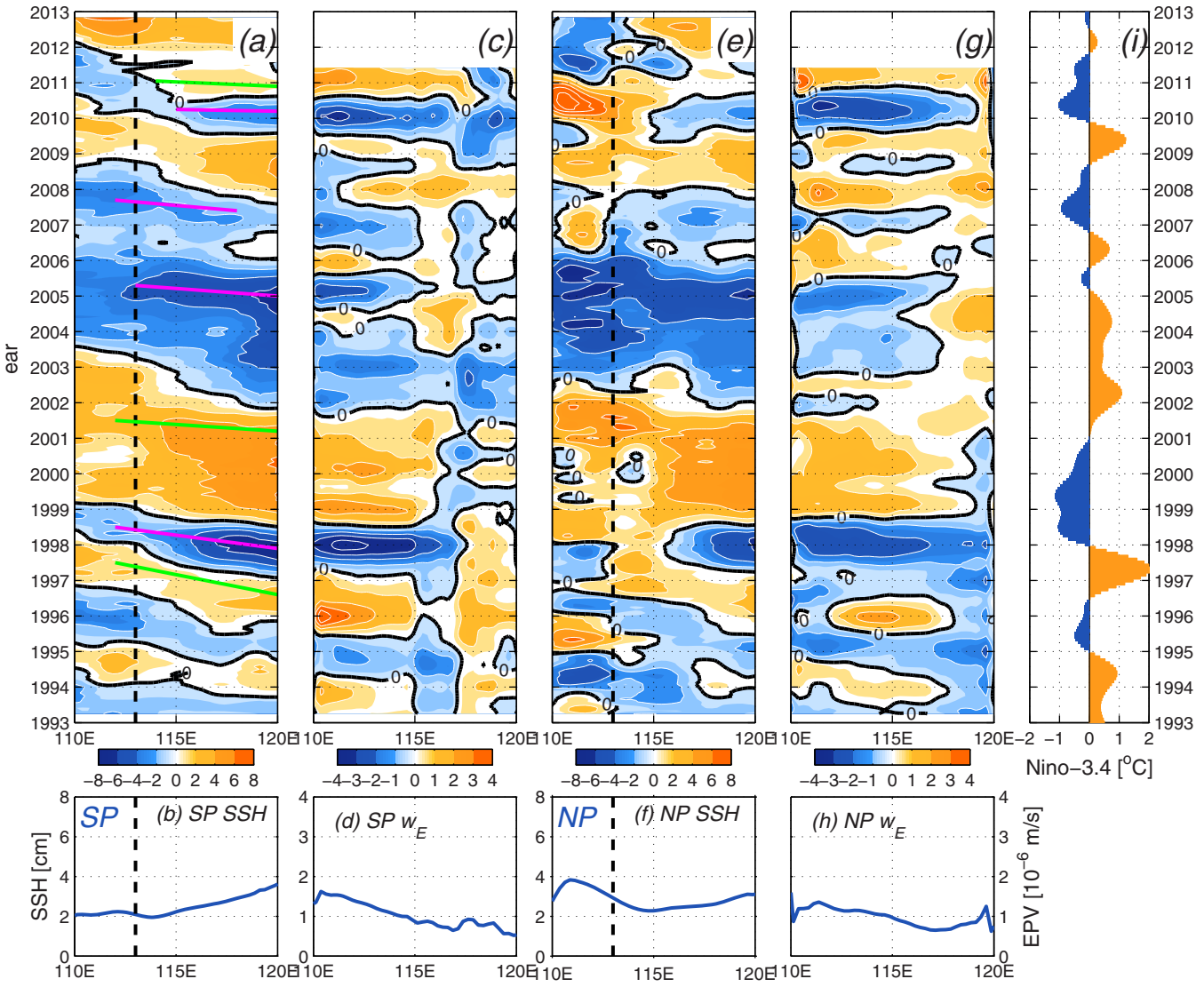

Figure 11. Time-longitude plots of (a) low-passed SSHA (cm) and (c) low-passed Ekman pumping velocity w_E anomaly (10^{-6} m s^{-1}) averaged between the latitude range of the SP (7.5°N–10.5°N). Figures 11b and 11d are the corresponding STD values of Figures 11a and 11b as functions of longitude. Figures 11e–11h are analogs of Figures 11a–11d but averaged between the latitude range of the NP (11°N–14°N). (i) Low-passed Niño-3.4 (°C) time series. In Figure 11a, the green (pink) lines indicate the propagation directions of positive (negative) SSHAs.

The propagation speeds of major signals range between 16 and 28 cm s^{-1} (green and pink lines), which are roughly consistent with the observed phase speed of the first baroclinic mode Rossby waves at these latitudes [e.g., *Kessler*, 1990; *Chelton and Schlax*, 1996]. The signals are significantly weakened as they progress westward, and the STD decreases from 3.8 cm at the eastern boundary to about 2.0 cm at 114°E (Figure 11b). Besides the damping by oceanic mixing and eddies, the weakened signal may also result from the cancelling effect of local wind forcing along the waveguide, due to the sign reversal of w_e anomaly between 115°E and 118°E (Figures 11c) around the Palawan Island (locations of Sulu Sea and Palawan Island are marked in Figure 1).

At low latitudes, low-frequency SSHAs are primarily signatures of first baroclinic mode Rossby waves induced by Ekman pumping [e.g., *Meyers*, 1979; *Chelton and Schlax*, 1996]. In a linear, 1.5 layer reduced-gravity model under long-wavelength approximation, the change of upper layer thickness h is governed by [e.g., *Meyers*, 1979; *Kessler*, 1990]

$$\frac{\partial h}{\partial t} + C_R \frac{\partial h}{\partial x} = -w_E, \tag{5}$$

where $C_R = -\beta c^2/f^2$ is the phase speed of long baroclinic Rossby wave, $\beta = \partial f/\partial y$ is the meridional gradient of f, and c is the phase speed of long baroclinic gravity wave. SSH variation in this model is related to h

change through $g\partial SSH/\partial t = g'\partial h/\partial t$ and $g\partial SSH/\partial x = g'\partial h/\partial x$, where g' is the reduced gravity parameter. In the linear system, interannual anomaly does not interact with the mean seasonal cycle. Therefore, equation (5) can be rewritten as [e.g., *Qiu and Chen*, 2010]

$$\frac{\partial SSHA}{\partial t} + C_R \frac{\partial SSHA}{\partial x} = -\frac{g'}{g} w'_E, \tag{6}$$

where w'_E is the interannual anomaly of Ekman pumping velocity. Equation (6) describes the relationship between SSHA and wind forcing. Then SSHA(x, t) can be solved by zonally integrating equation (6) from the eastern boundary x_e to x along the Rossby wave characteristic

$$SSHA(x,t) = -\frac{g'}{gC_R}\int_{x_e}^{x} w'_E\left(x', t - \frac{x-x'}{C_R}\right)dx' + SSHA\left(x_e, t - \frac{x-x_e}{C_R}\right). \tag{7}$$

Evidently, SSHA at x is determined by w_E forcing across the SCS basin (the first term on the right-hand side) and the eastern boundary signal (the second term on the right). Given the 16–28 cm s^{-1} C_R values, it takes only 2–3 months for Rossby waves to propagate from $x_e = 120°E$ to $x = 110°E$, which is much shorter than the interannual timescale we study. Therefore, interannual SSHA in the SCS is in a quasi-equilibrium state. Then equation (6) can be simplified into

$$SSHA(x) = -\frac{g'}{gC_R}\int_{x_e}^{x} w'_E(x')dx' + SSHA(x_e). \tag{8}$$

In this case, interannual SSHA in the SEJ region is determined by the zonal integral of w'_E (local wind forcing in the SCS) and eastern boundary signal SSHA (x_e). However, we need to bear in mind that equation (5) is based on linear and inviscid assumptions for steady ocean circulation. Oceanic internal variability due to nonlinearity can have strong influence (discussed in section 5.2), and both local wind forcing and SSHA(x_e) can be significantly modified by dissipation.

The importance of local wind forcing on SSHAs is visually identifiable in Figures 11a and 11c, supported by the significant simultaneous correlation between SP-averaged w_E and SSHAs ($r = -0.36$; >95% significance). Note that the SSHA amplitude and phase at the eastern boundary cannot be explained by the overlying wind forcing. Rather, they bear a close relationship with Niño-3.4 index (Figure 11i). Large negative SSHAs in 1994–1995, 1997–1998, 2002–2005, and 2009–2010 all occurred during warm ENSO phases, while positive ones in 1996, 1998–2001, 2008, and 2010–2011 appeared during cold ENSO phases. Sea level falling (rising) in the northwestern tropical Pacific during the warm (cold) ENSO phases has been reported by several studies [e.g., *Qiu and Chen*, 2010; *Li et al*., 2012; *Zhai and Hu*, 2013]. Part of these signals can transmit into the SCS through the Philippine archipelago [e.g., *Liu et al*., 2011; *Zhuang et al*., 2013] and affect SSH variability in the double-gyre area by radiating free Rossby waves.

At the NP latitudes, the westward propagations of SSHA are nearly undiscernible (Figures 11e). The lack of coherent propagating feature is likely due to the modification of the basin-scale w_E in the SCS on the eastern boundary signals (Figures 11g and 11h). SSHAs at eastern boundary always encounter zonally coherent w_E anomalies with the same sign. For example, positive SSHAs appear at the eastern boundary in 1995–1996, 1999–2002, 2008–2009, and 2010–2011, while positive w_E anomalies dominate in the SCS basin; negative SSHAs arise in 1994–1995, 1997–1998, 2002–2005, and 2009–2010, when negative w_E anomalies prevail. As a result, the SSHAs first weaken from the eastern boundary to 114°E and then rapidly intensify to a peak in the NP (Figure 11f), and SSHAs in the western SCS seem to be disconnected from the eastern boundary signals in most years. Consequently, the SSHAs in the NP result at least partly from local wind forcing in the SCS. Note that the eastern boundary signals for the SP and NP are similar, further suggesting their common origin from the western Pacific.

What is the relative importance of local wind forcing in the SCS and eastern boundary forcing? To quantify their relative contribution, we compare the dipole-area SSHA with zonal-averaged w_E anomaly (within the SCS), and eastern boundary SSHA in Figure 12. Theoretically, if SSHA in the dipole area is forced by local wind forcing within the SCS, it will have a negative correlation with the zonal-averaged w_E (positive w_E induces negative SSHA); if induced by eastern boundary forcing, it will have a lagged positive correlation with the eastern boundary SSHA. The eastern boundary SSHA (118°E–120°E, 7.5°N–10.5°N) has larger amplitude

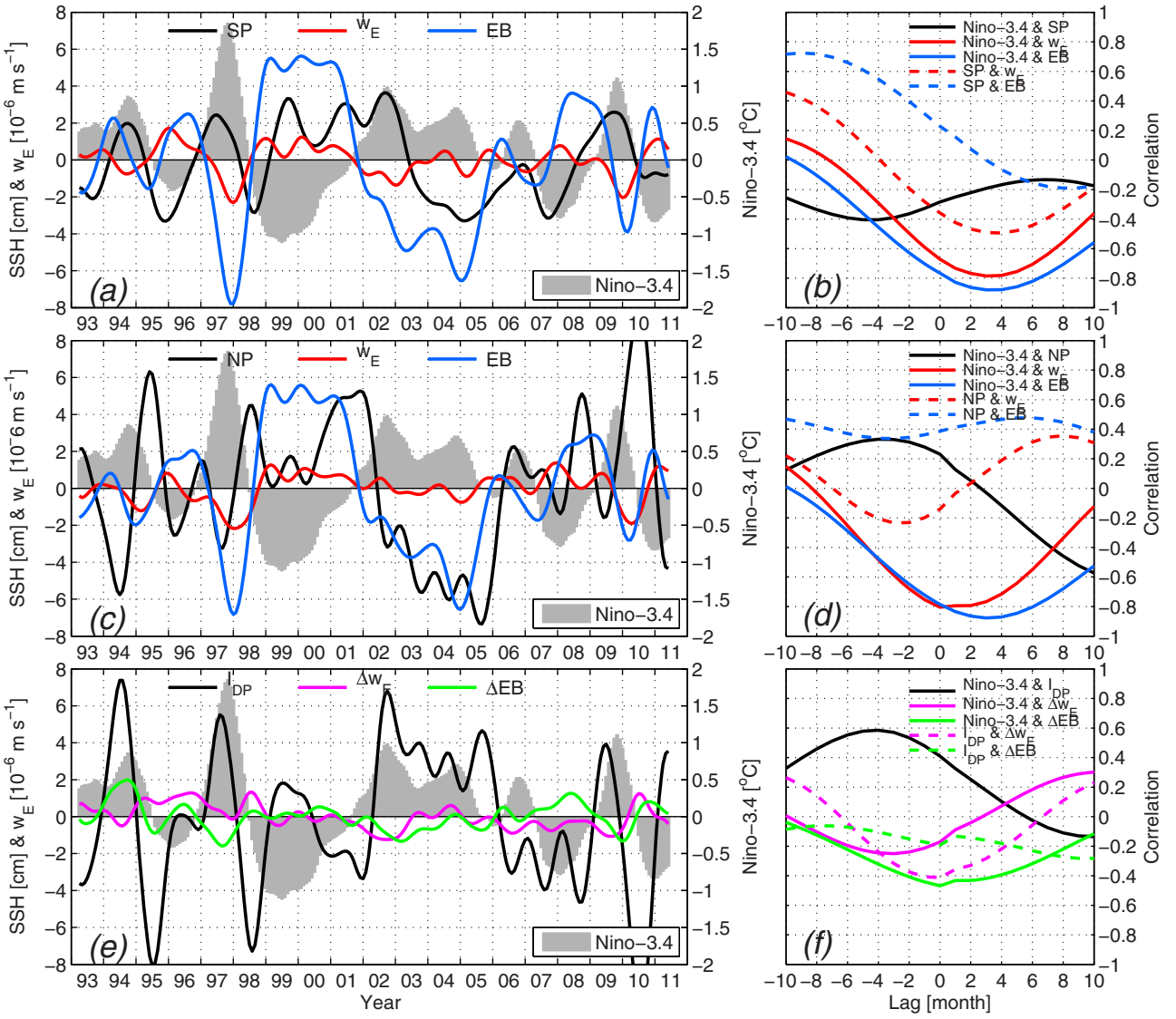

Figure 12. (a) Time series of low-passed SSHA (black; in cm), zonally averaged w_E anomaly (red; 10^{-6} m s^{-1}), and the eastern boundary (EB) SSHA (blue; 118°E–120°E) for the SP, together with Niño-3.4 (gray bars). (b) Lead-lag correlations of Niño-3.4 versus SP SSHA (black solid), Niño-3.4 versus SP w_E (red solid), Niño-3.4 versus eastern boundary SSHA (blue solid), SP SSHA versus w_E (red-dashed), and SP SSHA versus eastern boundary SSHA (blue-dashed). A positive lag for the solid (dashed) curve indicates the leading by Niño-3.4 (SP SSHA). Figures 12c and 12d are analogs of Figures 12a and 12b, but for the NP. Figures 12e and 12f are also analogs to Figures 12a and 12b, but for I_{DP} (black), the SP/NP difference of the zonally averaged w_E anomaly Δw_E (pink), and the SP/NP difference of the eastern boundary SSHA (green). A positive lag for a solid (dashed) curve indicates the leading by Niño-3.4 (I_{DP}).

and a significant leading relationship with the SP SSHA ($r = 0.39$–0.73 at 2–10 months leading), while the out-of-phase relationship between SP SSHA and w_E is also evident ($r = -0.36$ at 0 lag) (Figures 12a and 12b). The SSHAs in the NP have lower correlations with w_E anomalies and eastern boundary signals (Figures 12c and 12d). The eastern boundary SSHA shows a correlation value of 0.35–0.45 with several months' leading, while w_E has a correlation of -0.23 at 2–3 months leading. These results suggest that both local wind forcing and eastern boundary influence SSHAs in the dipole area. Due to the superimposition of the two effects and the modification of dissipation, the leading time is not strictly in line with the time of Rossby wave propagation. It is interesting to note that while the eastern boundary SSHAs are similar between the two latitude ranges (blue curves in Figures 12a and 12c), SSHAs in the SP and NP are markedly different (black curves in Figures 12a and 12c). This implies that the eastern boundary forcing cannot induce the change of the SSH difference between the SP and NP, i.e., I_{DP}.

To explore the cause for I_{DP} variations, we compute the meridional difference (SP minus NP) of the zonal-averaged w_E and eastern boundary SSHA, Δw_E and ΔEB (Figures 12e and 12f). The definition of Δw_E is in

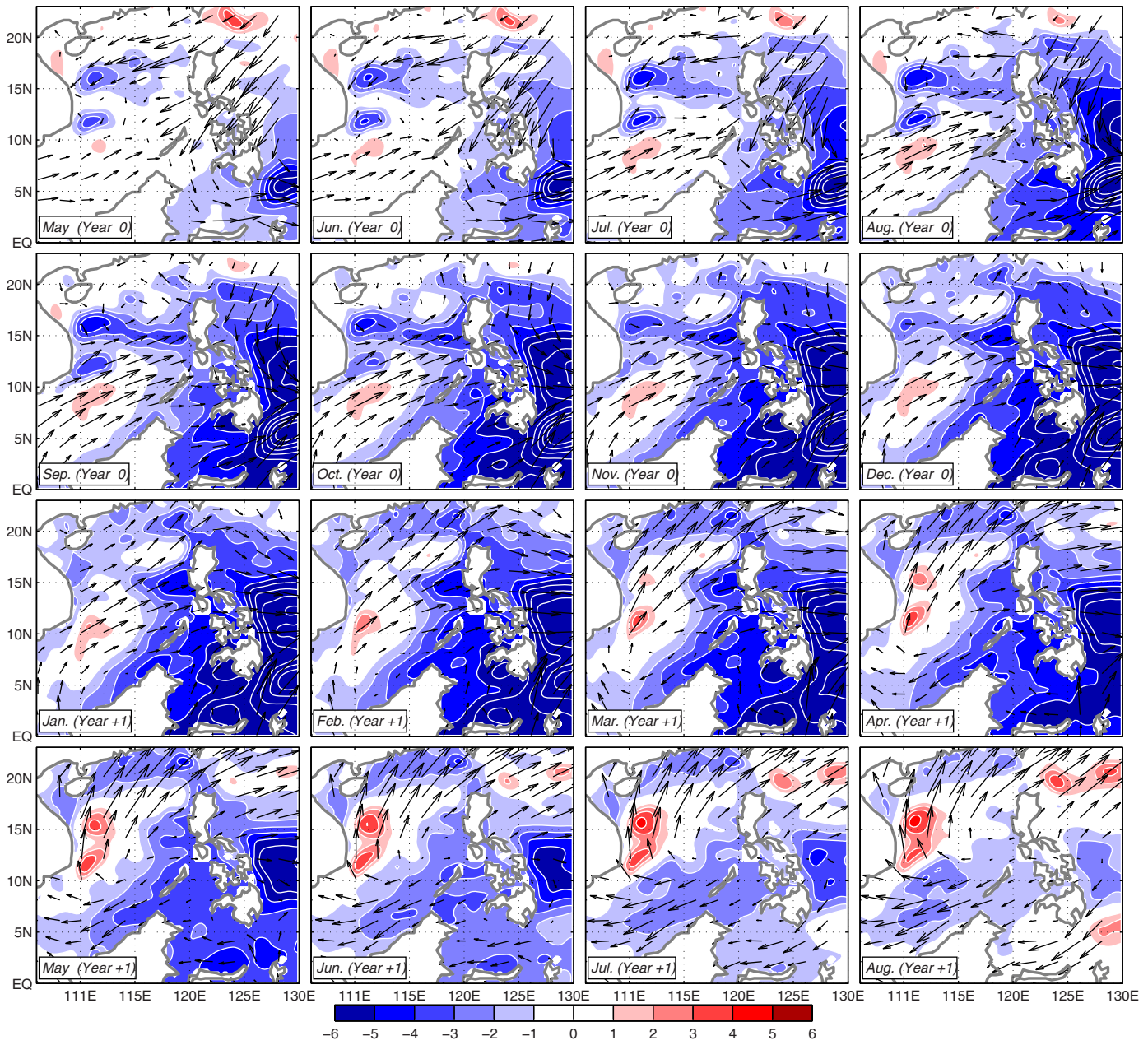

Figure 13. Monthly low-passed SSHA (color shading; in cm) and wind stress anomaly (vectors; in N m^{-2}) maps of the composite El Niño event from May Year 0 to August Year +1.

fact very similar to the SCS monsoon index proposed by *Wang et al.* [2009], except that we use w_E instead of wind stress shear. Hence, Δw_E is also a measure of the summer monsoon strength. Δw_E shows an $r = -0.42$ correlation (>95% significance) with I_{DP} at a 1 month leading. On the other hand, the correlation with ΔEB is negative and not significant. Therefore, eastern boundary signals cannot be responsible for the change of I_{DP}. These results confirm that local wind forcing, i.e., the strength of the southwest monsoon, is the primary cause of the interannual variability of the SEJ through a meridional dipole mode of SSHA, which is consistent with our analysis in section 4.1. Remote wind effect from the tropical Pacific can also modulate SSH variations in the western SCS through eastern boundary forcing, but its impact on I_{DP} and the SEJ is small. Even though monsoon wind is important, its correlation with I_{DP} is not very large (−0.42), implying the possible impact from other processes which will be discussed in section 5.

4.3. Effect of ENSO

Existing studies suggest that ENSO is the primary cause for the interannual variations of the East-Asian monsoon [e.g., *Tomita and Yasunari*, 1996; *Wang et al*., 2000, 2009] and sea level in the SCS [*Fang et al*., 2006; *Rong et al*., 2007; *Chang et al*., 2008]. Among others, *Chang et al*. [2008] showed that ENSO can induce a meridional dipole of SSHA that resembles Figures 9a and 9b in the summer SCS. To examine the ENSO impact on the SEJ, we conduct a composite El Niño event by six warm events with Niño-3.4 anomaly exceeding 0.7 STD value (1994–1995, 1997–1998, 2002–2003, 2004–2005, 2006–2007, and 2009–2010). Because the mature phase of El Niño usually occurs in winter, each event consists of a developing year (Year 0) and a decaying year (Year +1). The low-passed SSHA and wind anomalies are averaged for each month of the 2 year composite (Figure 13). In Year 0, anomalous southwesterly winds arise first in the southern SCS in spring and then get fully developed in summer. The enhanced SCS southwest monsoon at the developing phase of El Niño leads to a meridional dipole SSHA pattern resembling Figure 9a and hence a positive I_{DP}. In the decaying phase (Year +1), the entire SCS is under a large-scale surface wind anticyclone [*Wang et al*., 2000]. Northeasterly winds on the southern flank of this anticyclone get fully developed in the summer of Year +1, suppressing the mean southwest monsoon and giving rise to a SSHA pattern similar to Figure 9b and hence a negative I_{DP}. Regarding the robustness of the composite analysis, we also checked the individual events. In five of the six events, summer monsoon at the developing year is significantly stronger than the following decaying year. The only exception is the weak 2004–2005 event, during which monsoon intensity is similar in 2004 and 2005.

The prominent impact from ENSO is also supported by lead-lag correlations. Nino-3.4 index has significant correlations (correlation magnitude >0.79) with eastern boundary SSHA and w_E at both SP and NP latitudes (Figures 12b and 12d). However, its direct correlations with SP and NP SSHAs are relatively low ($r = -0.41$ at a 5 month leading in the SP and $r = 0.36$ at 4 month leading in the NP). This is likely due to the combination of the local wind forcing and eastern boundary signals and eddy influence. On the other hand, I_{DP} has positive correlation of $r = 0.60$ at 4 months leading and a negative 9 month lagged correlation with Niño-3.4 (Figure 12f), reflecting the relationship that a positive (negative) SSHA dipole emerges in the summer of the developing (decaying) year of an El Niño. Therefore, the effect of ENSO can be summarized as follows: the enhanced southwest monsoon at the developing phase of an El Niño induces a positive I_{DP} (positive SSHAs at the SP and negative SSHAs in the NP) and leads to a strong, southward shifted SEJ, and the weakened monsoon at the decaying phase of an El Niño induces a negative I_{DP} and leads to a weak, northward shifted SEJ. This also explains why there exists a tendency for a strong, southward shifted SEJ followed by a weak, northward shifted one.

5. Discussion

5.1. The 2010 Case

The 2010 disappearance case occurred at the decaying stage of the 2009–2010 El Niño when the southwest monsoon was extremely weak. However, I_{DP} value in 2010 is similar to that in 1998, which is influenced by the strong 1997–1998 El Niño. In 1998 we can still identify an organized SEJ structure near the Vietnam coast. The SEJ disappearance in 2010 therefore cannot be explained by the processes proposed in section 4. Comparing the surface wind patterns of 1998 and 2010 (Figures 14a and 14b), we can see that the northward component of the wind jet near the Vietnam coast is stronger in 2010. As a result, larger positive (negative) w_E anomalies occur on the inshore (offshore) side of the wind jet between 12°N and 16°N, which leads to a SSH decrease (elevation) on the inshore (offshore) side. This anomalous SSH gradient drives northward alongshore geostrophic flow near the Vietnam coast, rather than produces an offshore separation of the Vietnam coastal current (Figure 5). The diverse wind patterns between 1998 and 2010 may be related to event-to-event differences of El Niños [e.g., *Larkin and Harrison*, 2005; *Ashok et al*., 2007; *Kug et al*., 2009]. The 1997–1998 event is the strongest classical-type (eastern-Pacific) El Niño in the 20th century (Figure 14c), while the 2009–2010 event is the strongest central-Pacific El Niño in the oceanographic record (Figure 14d) [*Lee and McPhaden*, 2010]. The two types of El Niños can have different effects on the SCS wind and sea level [*Chang et al*., 2008].

During strong post-El Niño summers, such as 1995 and 1998, the cyclonic gyre of the double-gyre structure shifts to 14°N–16°N, which allows the SEJ to be formed on its southern side (Figure 5). In 2010, however,

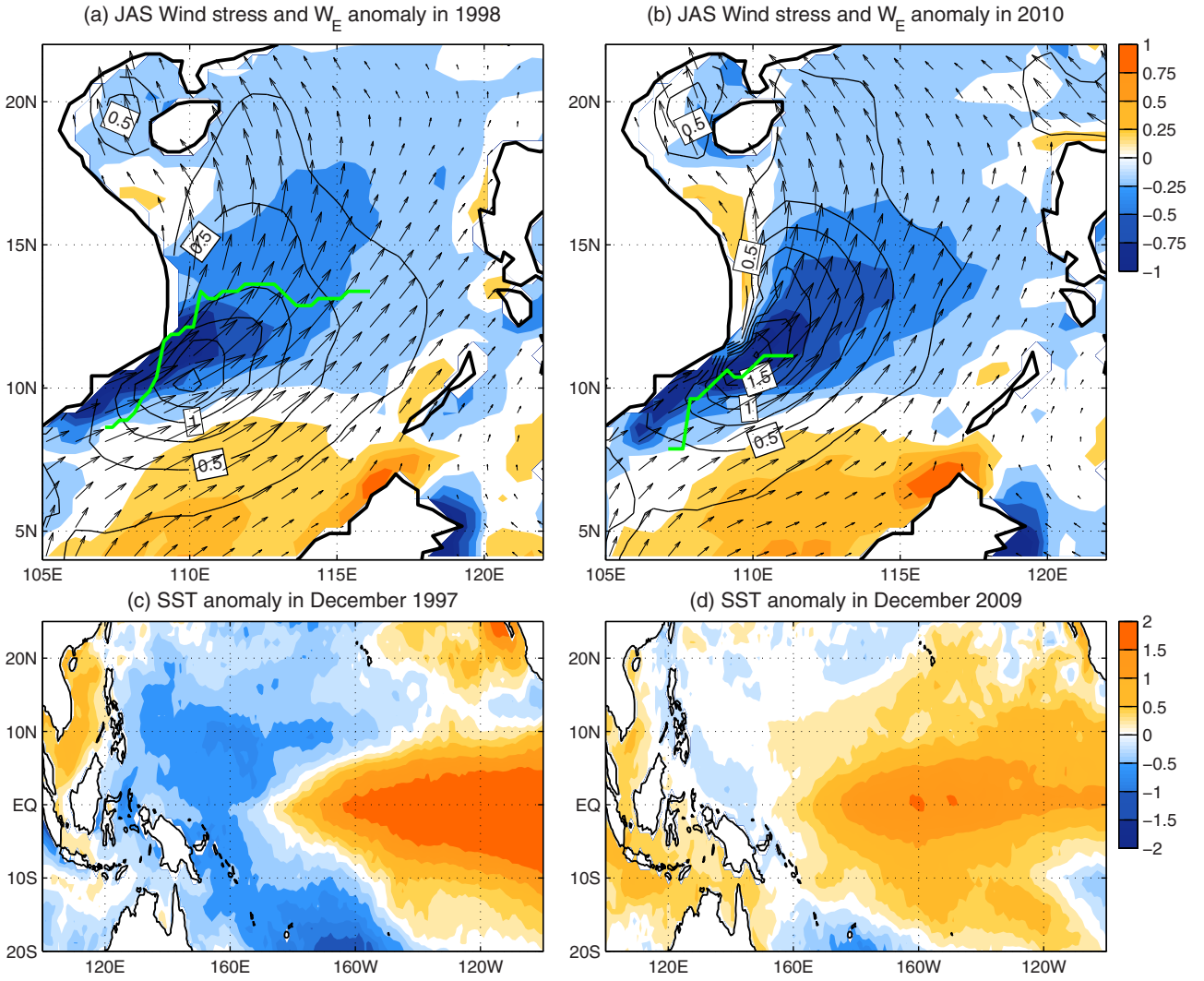

Figure 14. JAS-mean wind stress (black vector and contours; in 10^{-2} N m^{-2}) and w_E anomaly (color shading; in 10^{-6} m s^{-1}) in (a) 1998 and (b) 2010, with the green curve denoting the Y_{SEJ}. Low-passed SST anomaly (°C) in (c) December 1997 and (d) December 2009.

the entire mid-to-northern SCS is occupied by a strikingly strong basin-scale anticyclonic gyre [*Chu et al.*, 2014]. The main flow of the Vietnam coastal current joins this anticyclonic gyre as the western boundary current, instead of separating from the coast to feed the SEJ. Time-longitude map of low-passed SSHA between 14°N and 16°N shows strikingly large SSHA in 2010, which denies the formation of the cyclonic gyre appeared in others years (Figure 15b). The large negative w_E anomaly in that year (Figure 15c) clearly contributes to the formation of the large SSHA. Besides, in 1998, there are large negative SSHAs at the eastern boundary, which can partly compensate for the positive SSHAs produced by negative w_E. In 2010, however, the eastern boundary signals are much weaker. These features work together to produce the high sea level in the western SCS (Figure 15a).

Except for the 1997–1998 event, most of the El Niños during the past two decades are classified as central-Pacific events according to existing studies [e.g., *Ashok et al.*, 2007; *Kug et al.*, 2009; *Hsin and Qiu*, 2012]. Other central-Pacific events however did not result in the disappearance of the SEJ as in 2010, likely because their amplitude and teleconnection are not strong enough as the 2010 event (Figure 15d). As the strongest central-Pacific warming event in the oceanographic record, the 2009–2010 El Niño has many strong and unique remote effects on the global climate [e.g., *Lee and McPhaden*, 2010]. One can see in Figure 7 that the southwest monsoon is remarkably weak in 2010 compared with other postevent years such as 1995, 2003, 2005, and 2007. As a result, the sea level response in the western SCS is much stronger in 2010 (Figures 15a and 15b), which leads to the disappearance of the SEJ.

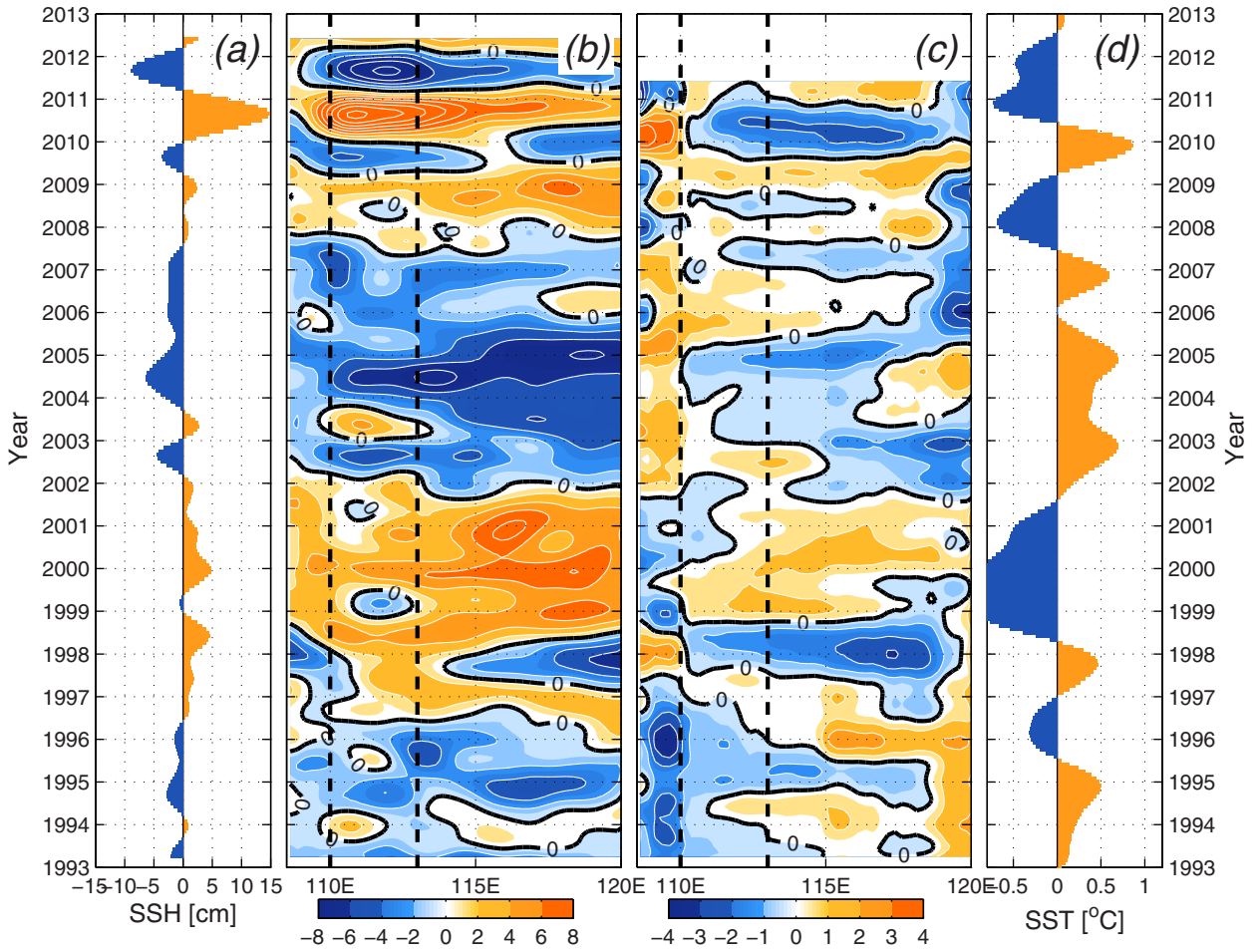

Figure 15. (a) Mean low-passed SSHA between 110°E and 113°E, 14°N and 16°N. Time-longitude plots of (b) low-passed SSHA (cm) and (c) low-passed w_E anomaly (10^{-6} m s^{-1}) averaged between 14°N and 16°N. (d) Low-passed SST anomaly averaged over the central Pacific region (165°E–140°W, 10°S–10°N).

In this study we addressed merely the impact of ENSO, which can explain the majority of the observed variations. However, the possible impact from the Indian Ocean, such as the Indian dipole mode, is unknown. Recent studies showed that the air-sea interaction in the tropical Indian Ocean may affect the intensity of the East Asian summer monsoon though atmospheric teleconnection [e.g., *Kripalani et al.*, 2005; *Du et al.*, 2009; *Xie et al.*, 2009] and modulate the SST variability in the SCS [e.g., *C. Wang et al.*, 2006]. This process could be an important complement to the ENSO-monsoon teleconnection stressed in the study. In addition to wind forcing and linear ocean response, we cannot exclude the possibility that nonlinear ocean processes are involved in the development of this strong anticyclonic gyre in the mid-to-northern SCS.

5.2. Ocean Internal Variability

Analysis in section 4 has more than once indicated the impact of ocean internal variability. This speculation arises also from the strikingly high mesoscale eddy activity in the western SCS [e.g., *Wang et al.*, 2003; *Chen et al.*, 2010, 2011; *Zhuang et al.*, 2010]. The complicated eddy-mean flow interaction can have a considerable impact on the large-scale mean flow variability. Because of its complexity, it is difficult to assess the effect of ocean internal variability using observational data. We therefore analyze the OGCM experiment results. To check the model performance in reproducing the mesoscale eddy variability, eddy kinetic energy (EKE) is estimated with both AVISO U_G and HYCOM surface U through EKE $= U'^2/2 + V'^2/2$, where U' and V' is the zonal and meridional current perturbation obtained with a 140 day high-pass filter. The spatial structure and typical value of JAS-mean EKE from the HYCOM output are quite close to those from AVISO data (Figures 16a and 16b). More importantly, the model can well reproduce the temporal variability of EKE averaged

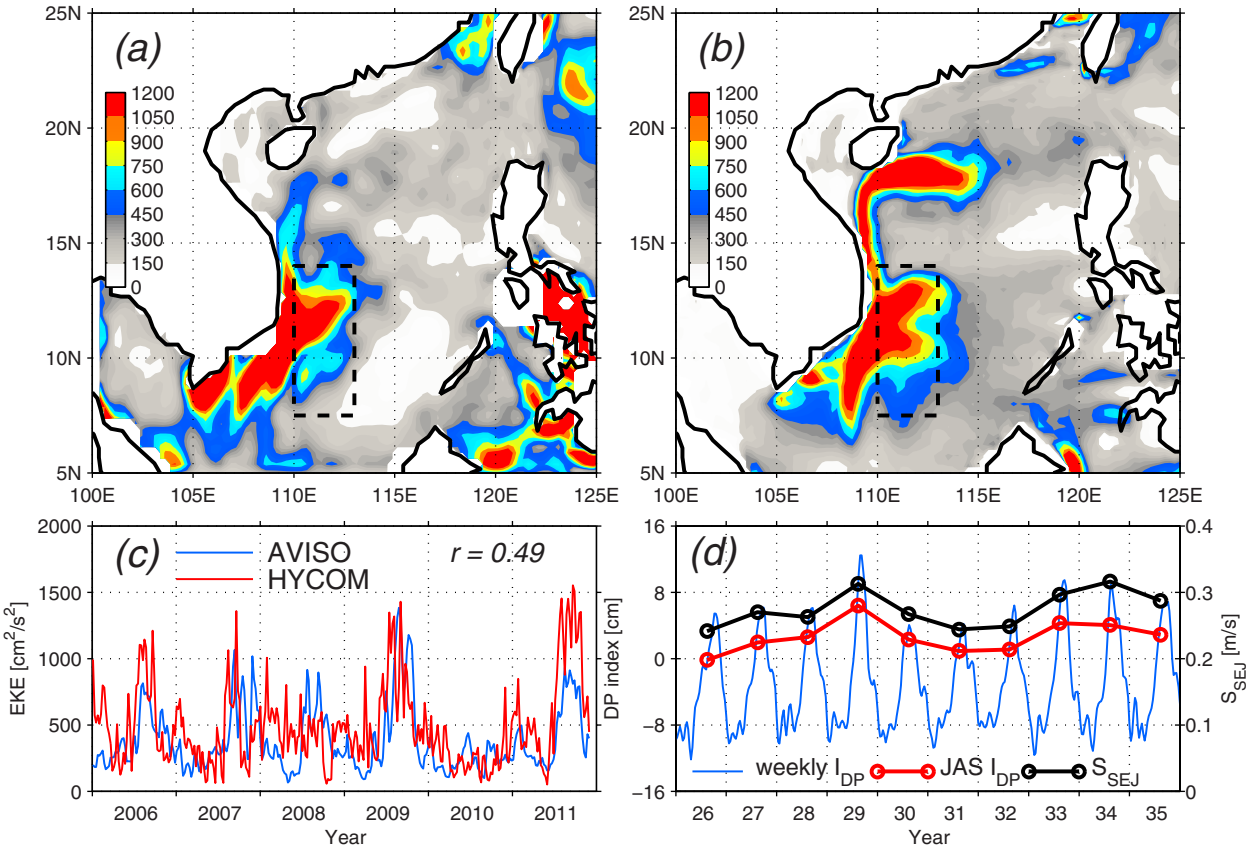

Figure 16. Mean JAS eddy kinetic energy (EKE; in $cm^2\ s^{-2}$) during 2006–2011 from (a) AVISO and (b) HYCOM control run. The dashed rectangle denotes the dipole area. (c) Weekly EKE time series based on AVISO surface geostrophic current (blue) and HYCOM control run surface current (red). (d) Weekly time series of I_{DP} (blue; in cm) and its yearly JAS-mean version (red) and yearly JAS-mean surface SEJ strength S_{SEJ} (black; in m s^{-1}) based on the 26th–35th year record of the HYCOM climatologic run.

over the SEJ and dipole area (Figure 16c), including the seasonal cycle and the year-to-year changes. Note that EKE is calculated with weekly data. The $r = 0.49$ correlation is very significant (99% confidence level assuming each weekly sample is independent). Such good accordance implies that the model is able to capture the ocean internal processes (such as barotropic and baroclinic instabilities) that produce mesoscale eddies.

The effect of the ocean internal variability can be assessed with the output of the HYCOM climatologic run, which is forced by monthly climatologic atmospheric fields. Therefore, this simulation contains no forced interannual variation, and all the year-to-year changes arise from ocean internal processes such as the eddy-current interaction. The climatologic run has achieved a stable state since the 15th year of the spin-up. We use the SSH record of the last 10 years (26th–35th year). The I_{DP} index estimated from these SSH record shows evident year-to-year changes superimposed on a seasonal cycle. The JAS-mean I_{DP} has a typical peak-to-peak difference of 7 cm (Figure 16d), equivalent to about 20% of that of the observed I_{DP} ($\sim$35 cm). Correspondingly, the modeled S_{SEJ} in the climatologic run shows changes with typical difference of 0.07 m s^{-1}, which equals to $\sim$18% of the observed value (0.38 m s^{-1}). This result suggests that except the wind forcing and linear oceanic response, a considerable portion of the low-frequency SSH and current variance is caused by ocean internal processes.

Here only I_{DP} and S_{SEJ} changes are examined with the HYCOM results, because the model cannot reproduce the observed meridional displacements of the SEJ. The modeled Y_{SEJ} exhibits very weak year-to-year fluctuations ($<0.3°$). This may be related with the model bias in the northern SCS. The overstrong Kuroshio loop and recirculation gyre there may act to impede the northward shift of the SEJ. We have also examined the results of other models, the 0.1°-resolving OFES, the 7 km ROMS configured for the SCS, and a 5 km CT-ROMS. All of them are with eddy-resolving spatial resolutions, and the two ROMS simulations include river

discharge and tidal forcing. However, even these state-of-the-art global and regional OGCMs fail to realistically present the meridional displacements of the SEJ position. Our results in this study suggest a complex mechanism governing the circulation variability in this region. Even within the wind forcing-linear response mechanism, we have only roughly estimated the relative contribution of the local wind forcing and eastern boundary forcing with observational data. An unambiguous examination for this issue can only be achieved through model experiments isolating the two effects. Investigation should be continued with more observational data and further improved models in the future to gain more in-depth understanding.

6. Summary

As the offshore extension of the Vietnam coastal current, the SEJ is an important current of the summertime SCS surface circulation. The mean SEJ is seen at 12°N, 110°E–113°E with surface velocities >0.5 m s^{-1} and accompanied by a double-gyre structure. It transports the cold water from coastal upwelling zone eastward to the interior basin and is potentially important for basin-scale SST and regional climate variability. In this study, we investigate the interannual variations of the surface SEJ using satellite sea level and surface wind data from 1992 through 2012 in conjunction with OGCM experiments.

During 1992–2012, the SEJ exhibits pronounced interannual variations in both its surface strength S_{SEJ} and latitudinal position Y_{SEJ}. In most years, the JAS-mean S_{SEJ} averaged between 110° and 113° varies from 0.17 to 0.55 m s^{-1}, while Y_{SEJ} fluctuates between 10.7° and 14.3°N. An exception occurred in 2010, with no organized SEJ structure identified near the Vietnam coast. Geostrophic current dominates the SEJ variations, while the Ekman component is one order weaker. The year-to-year variations of the SEJ are significantly correlated with the changes of sea surface wind over the SCS basin. Both S_{SEJ} and Y_{SEJ} show high correlations with the strength of the southwest monsoon. Enhanced southwest monsoon leads to a stronger, southward shifted SEJ, while weakened southwest monsoon leads to a weaker, northward shifted SEJ.

A meridional dipole pattern of SSHA is found to be a critical link between the wind forcing and the SEJ variability. We use the dipole index I_{DP} to quantify this SSHA mode, which is shown to be a good proxy for both S_{SEJ} and Y_{SEJ}. The SSHAs associated with the I_{DP} are primarily caused by ENSO variability, which produces the low-frequency SCS SSHAs through both local wind forcing within the SCS (strength changes of the southwest monsoon) and the eastern boundary forcing. The latter conveys SSHA signals from the western Pacific to the SCS through the Philippine Archipelago. However, the eastern boundary forcing only affects the overall sea level over the dipole region, and it does not act to modify the SSH difference between the SP and NP, and its impact on I_{DP} and the SEJ is therefore negligible. Variations of I_{DP} and the SEJ are primarily induced by SCS wind forcing through Ekman pumping. Enhanced (weakened) southwest monsoon at the developing (decaying) stage of an El Niño event causes a stronger (weaker) SEJ located south (north) of its mean position.

In 2010 when the SEJ disappears, the entire mid-to-northern SCS is dominated by a strong basinwide anticyclonic gyre with SSH higher than normal by 20–40 cm. Unique wind pattern and weak eastern boundary signals favors the formation of the high SSHA, which is likely related to a unique teleconnection signature of the 2009–2010 El Niño, with the strongest warming occurring in the central equatorial Pacific. Recent studies have suggested the increase of frequency and strength of central-Pacific Niños under the present global warming trend [*Yeh et al*., 2009; *Lee and McPhaden*, 2010]. This will further complicate the mechanism controlling the SCS regional circulation. On the other hand, it will also be interesting to have more samples of disappearance cases in the future, which will allow for a more in-depth investigation for such special cases.

We also assessed the impact of ocean internal variability using the HYCOM model. Results of the climatologic run show that ocean internal variability can induce interannual changes of 7 cm in I_{DP} and 0.07 m s^{-1} in S_{SEJ}. Such magnitude is equivalent to about 20% of the observed variations. Both the HYCOM and several other eddy-resolving OGCMs have great difficulties in simulating the meridional displaces of the SEJ. The considerable impact from the nonlinear ocean internal variability also suggests the complexity of the ocean dynamics in this region. Previous modeling studies indicate that even simulating the climatological state of the costal current separation and formation of the SEJ has been a challenging task for existing OGCMs [*Gan et al*., 2006; *Gan and Qu*, 2008; *Chen et al*., 2012]. In our results, the simulation of Y_{SEJ} variability is hindered by the unrealistically strong Kuroshio intrusion loop in the northern SCS. These model biases are primarily

due to the incompetence of models in representing the key dynamic processes. From this point of view, our investigation with available satellite observation is helpful for integrating our knowledge of the regional ocean dynamics and improving the model simulation.

Acknowledgments
This research was supported by the ONR grant N00014-12-1-03-23 and the NSF CAREER Award 0847605. Two anonymous reviewers provided useful comments and suggestions for improving our work. We appreciate the help from Office of Information Technology (OIT) of University of Colorado and the National Center for Atmospheric Research (NCAR) CISL for providing computational support. AVISO sea level product is downloaded from http://www.aviso.oceanobs.com/; CCMP sea surface wind data are downloaded from http://podaac.jpl.nasa.gov/; OSCAR ocean current data are available at http://podaac.jpl.nasa.gov/; NOAA OISST V2 data are taken from http://www.esrl.noaa.gov/; Niño-3.4 index is provided by the Climate Prediction Center of NOAA through http://www.cpc.ncep.noaa.gov.

References

Ashok, K., S. K. Behera, S. A. Rao, H. Weng, and T. Yamagata (2007), El Niño Modoki and its possible teleconnection, *J. Geophys. Res.*, *112*, C11007, doi:10.1029/2006JC003798.

Atlas, R., J. Ardizzone, and R. N. Hoffman (2008), Application of satellite surface wind data to ocean wind analysis, *Proc. SPIE 70870B*, *Remote Sensing System Engineering*, *7087*, doi:10.1117/12.795371.

Bombar, D., J. W. Dippner, H. N. Doan, L. N. Ngoc, I. Liskow, N. Loick-Wilde, and M. Voss (2010), Sources of new nitrogen in the Vietnamese upwelling region of the South China Sea, *J. Geophys. Res.*, *115*, C06018, doi:10.1029/2008JC005154.

Bonjean, F., and G. S. Lagerloef (2002), Diagnostic model and analysis of the surface currents in the tropical Pacific Ocean, *J. Phys. Oceanogr.*, *32*, 2938–2954.

Castruccio, F. S., E. N. Curchitser, and J. A. Kleypas (2013), A model for quantifying oceanic transport and mesoscale variability in the Coral Triangle of the Indonesian/Philippines Archipelago, *J. Geophys. Res. Oceans*, *118*, 6123–6144, doi:10.1002/2013JC009196.

Chang, C. W., H. H. Hsu, C. R. Wu, and W. J. Sheu (2008), Interannual mode of sea level in the South China Sea and the roles of El Niño and El Niño Modoki, *Geophys. Res. Lett.*, *35*, L03601, doi:10.1029/2007GL032562.

Chao, S.-Y., P.-T. Shaw, and S. Y. Wu (1996), El Niño modulation of the South China Sea circulation, *Prog. Oceanogr.*, *38*, 51–93.

Chelton, D. B., and M. G. Schlax (1996), Global observations of oceanic Rossby waves, *Science*, *272*(5259), 234–238.

Chen, C., Z. Lai, R. C. Beardsley, Q. Xu, H. Lin, and N. T. Viet (2012), Current separation and upwelling over the southeast shelf of Vietnam in the South China Sea, *J. Geophys. Res.*, *117*, C03033, doi:10.1029/2011JC007150.

Chen, G., Y. Hou, Q. Zhang, and X. Chu (2010), The eddy pair off eastern Vietnam: Interannual variability and impact on thermohaline structure, *Cont. Shelf Res.*, *30*, 715–723.

Chen, G., Y. Hou, and X. Chu (2011), Mesoscale eddies in the South China Sea: Mean properties, spatiotemporal variability, and impact on thermohaline structure, *J. Geophys. Res.*, *116*, C06018, doi:10.1029/2010JC006716.

Chen, G., P. Xiu, and F. Chai (2014), Physical and biological controls on the summer chlorophyll bloom to the east of Vietnam, *J. Oceanogr.*, *70*, 323–328.

Chu, P. C., N. L. Edmons, and C. Fan (1999), Dynamical mechanisms for the South China Sea seasonal circulation and thermohaline variabilities, *J. Phys. Oceanogr.*, *29*, 2971–2989.

Chu, X., H. Xue, Y. Qi, G. Chen, Q. Mao, D. Wang, and F. Chai (2014), An exceptional anticyclonic eddy in the South China Sea in 2010, *J. Geophys. Res. Oceans*, *119*, 881–897, doi:10.1002/2013JC009314.

Dee, D., S. Uppala, A. Simmons, P. Berrisford, P. Poli, S. Kobayashi, U. Andrae, M. Balmaseda, G. Balsamo, and P. Bauer (2011), The ERA-Interim reanalysis: Configuration and performance of the data assimilation system, *Q. J. R. Meteorol. Soc.*, *137*, 553–597.

Dibarboure, G., O. Lauret, F. Mertz, V. Rosmorduc, and C. Maheu (2008), SSALTO/DUACS user handbook: (M)SLA and (M)ADT near-real time and delayed time products, *Rep. CLS-DOS-NT-06.034*, 39 p., Aviso Altimetry, Ramonville St. Agne, France.

Dippner, J. W., K. V. Nguyen, H. Hein, T. Ohde, and N. Loick (2007), Monsoon-induced upwelling off the Vietnamese coast, *Ocean Dyn.*, *57*(1), 46–62.

Dippner, J. W., D. Bombar, N. Loick-Wilde, M. Voss, and A. Subramaniam (2013), Comment on "Current separation and upwelling over the southeast shelf of Vietnam in the South China Sea" by Chen et al., *J. Geophys. Res. Oceans*, *118*, 1618–1623, doi:10.1002/jgrc.20118.

Du, Y., and T. Qu (2010), Three inflow pathways of the Indonesian throughflow as seen from the simple ocean data assimilation, *Dyn. Atmos. Oceans*, *50*, 233–256.

Du, Y., S.-P. Xie, G. Huang, and K. Hu (2009), Role of air–sea interaction in the long persistence of El Niño–induced North Indian Ocean warming, *J. Clim.*, *22*, 2023–2038.

Ducet, N., P. Le Traon, and G. Reverdin (2000), Global high-resolution mapping of ocean circulation from TOPEX/Poseidon and ERS-1 and-2, *J. Geophys. Res.*, *105*(C8), 19,477–19,498.

Ekman, V. W. (1905), On the influence of the Earth's rotation on ocean currents, *Arkiv Math. Astron. Fys.*, *2*, 1–53.

Fang, G., H. Chen, Z. Wei, Y. Wang, X. Wang, and C. Li (2006), Trends and interannual variability of the South China Sea surface winds, surface height, and surface temperature in the recent decade, *J. Geophys. Res.*, *111*, C11S16, doi:10.1029/2005JC003276.

Fang, G., Y. Wang, Z. Wei, Y. Fang, F. Qiao, and X. Hu (2009), Interocean circulation and heat and freshwater budouble gyreets of the South China Sea based on a numerical model, *Dyn. Atmos. Oceans*, *47*, 55–72.

Fang, W., G. Fang, P. Shi, Q. Huang, and Q. Xie (2002), Seasonal structures of upper layer circulation in the southern South China Sea from in situ observations, *J. Geophys. Res.*, *107*(C11), 3202, doi:10.1029/2002JC001343.

Gan, J., and T. Qu (2008), Coastal jet separation and associated flow variability in the southwest South China Sea, *Deep Sea Res., Part I*, *55*, 1–19.

Gan, J., H. Li, E. Curchitser, and D. Haidvogel (2006), Modeling South China Sea circulation: Response to seasonal forcing regimes, *J. Geophys. Res.*, *111*, C06034, doi:10.1029/2005JC003298.

Hai, D. N., N. N. Lam, and J. W. Dippner (2010), Development of *Phaeocystis globosa* blooms in the upwelling waters of the south central coast of Vietnam, *J. Mar. Sci.*, *83*, 253–261.

Han, W., A. M. Moore, J. Levin, B. Zhang, H. G. Arango, E. Curchitser, E. Di Lorenzo, A. L. Gordon, and J. Lin (2009), Seasonal surface ocean circulation and dynamics in the Philippine Archipelago region during 2004–2008, *Dyn. Atmos. Oceans*, *47*, 114–137.

Hsin, Y.-C., and B. Qiu (2012), The impact of Eastern-Pacific versus Central-Pacific El Niños on the North Equatorial Countercurrent in the Pacific Ocean, *J. Geophys. Res.*, *117*, C11017, doi:10.1029/2012JC008362.

Kessler, W. S. (1990), Observations of long Rossby waves in the northern tropical Pacific, *J. Geophys. Res.*, *95*(C4), 5183–5217.

Kripalani, R., J.-H. Oh, J.-H. Kang, S. Sabade, and A. Kulkarni (2005), Extreme monsoons over East Asia: Possible role of Indian Ocean zonal mode, *Theor. Appl. Climatol.*, *82*, 81–94.

Kug, J. S., F. F. Jin, and S. I. An (2009), Two types of El Niño events: Cold tongue El Niño and warm pool El Niño, *J. Clim.*, *22*(6), 1499–1515.

Kummerow, C., W. Barnes, T. Kozu, J. Shiue, and J. Simpson (1998), The tropical rainfall measuring mission (TRMM) sensor package, *J. Atmos. Oceanic Technol.*, *15*, 809–817.

Kuo, N.-J., Q. Zheng, and C.-R. Ho (2000), Satellite observation of upwelling along the western coast of the South China Sea, *Remote Sens. Environ.*, *74*, 463–470.

Larkin, N. K., and D. E. Harrison (2005), On the definition of El Niño and associated seasonal average U. S. weather anomalies, *Geophys. Res. Lett.*, *32*, L13705, doi:10.1029/2005GL022738.
Le Traon, P., F. Nadal, and N. Ducet (1998), An improved mapping method of multisatellite altimeter data, *J. Atmos. Oceanic Technol.*, *15*, 522–534.
Lee, T., and M. J. McPhaden (2010), Increasing intensity of El Niño in the Central-equatorial Pacific, *Geophys. Res. Lett.*, *37*, L14603, doi: 10.1029/2010GL044007.
Li, Y., F. Wang, and F. Zhai (2012), Interannual variations of subsurface spiciness in the Philippine Sea: Observations and mechanism, *J. Phys. Oceanogr.*, *42*, 1022–1038.
Li, Y., W. Han, T. Shinoda, C. Wang, R. C. Lien, J. N. Moum, and J. W. Wang (2013), Effects of the diurnal cycle in solar radiation on the tropical Indian Ocean mixed layer variability during wintertime Madden-Julian Oscillations, *J. Geophys. Res. Oceans*, *118*, 4945–4964, doi: 10.1002/jgrc.20395.
Liu, Q., M. Feng, and D. Wang (2011), ENSO-induced interannual variability in the southeastern South China Sea, *J. Oceanogr.*, *67*, 127–133.
Liu, X., J. Wang, X. Cheng, and Y. Du (2012), Abnormal upwelling and chlorophyll-a concentration off South Vietnam in summer 2007, *J. Geophys. Res.*, *117*, C07021, doi:10.1029/2012JC008052.
Liu, Z., H. Yang, and Q. Liu (2001), Regional dynamics of seasonal variability in the South China Sea, *J. Phys. Oceanogr.*, *31*, 272–284.
Madsen, O. S. (1977), A realistic model of the wind-induced Ekman boundary layer, *J. Phys. Oceanogr.*, *7*, 248–255.
Masumoto, Y., et al. (2004), A fifty-year eddy-resolving simulation of the World Ocean—Preliminary outcomes of OFES (OGCM for the Earth Simulator), *J. Earth Simul.*, *1*, 35–56.
Metzger, E. J., and H. E. Hurlburt (1996), Coupled dynamics of the South China Sea, the Sulu Sea, and the Pacific Ocean, *J. Geophys. Res.*, *101*(C5), 12,331–12,352.
Meyers, G. (1979), On the annual Rossby wave in the tropical North Pacific Ocean, *J. Phys. Oceanogr.*, *9*, 663–674.
Qiu, B., and S. Chen (2010), Interannual-to-decadal variability in the bifurcation of the North Equatorial Current off the Philippines, *J. Phys. Oceanogr.*, *40*, 2525–2538.
Qu, T. (2000), Upper-layer circulation in the South China Sea, *J. Phys. Oceanogr.*, *30*, 1450–1460.
Qu, T. (2001), Role of ocean dynamics in determining the mean seasonal cycle of the South China Sea surface temperature, *J. Geophys. Res.*, *106*(C4), 6943–6955, doi:10.1029/2000JC000479.
Qu, T., Y. Y. Kim, M. Yaremchuk, T. Tozuka, A. Ishida, and T. Yamagata (2004), Can Luzon Strait transport play a role in conveying the impact of ENSO to the South China Sea?, *J. Clim.*, *17*, 3644–3657.
Qu, T., Y. Du, G. Meyers, A. Ishida, and D. Wang (2005), Connecting the tropical Pacific with Indian Ocean through South China Sea, *Geophys. Res. Lett.*, *32*, L24609, doi:10.1029/2005GL024698.
Qu, T., Y. Du, and H. Sasaki (2006), South China Sea throughflow: A heat and freshwater conveyor, *Geophys. Res. Lett.*, *33*, L23617, doi: 10.1029/2006GL028350.
Qu, T., Y. T. Song, and T. Yamagata (2009), An introduction to the South China Sea throughflow: Its dynamics, variability, and application for climate, *Dyn. Atmos. Oceans*, *47*, 3–14.
Ralph, E. A., and P. P. Niiler (1999), Wind-driven currents in the tropical Pacific, *J. Phys. Oceanogr.*, *29*, 2121–2129.
Reynolds, R. W., T. M. Smith, C. Liu, D. B. Chelton, K. S. Casey, and M. G. Schlax (2007), Daily high-resolution-blended analyses for sea surface temperature, *J. Clim.*, *20*, 5473–5496.
Rio, M. H., S. Guinehut, and G. Larnicol (2011), New CNES-CLS09 global mean dynamic topography computed from the combination of GRACE data, altimetry, and in situ measurements, *J. Geophys. Res.*, *116*, C07018, doi:10.1029/2010JC006505.
Rong, Z., Y. Liu, H. Zong, and Y. Cheng (2007), Interannual sea level variability in the South China Sea and its response to ENSO, *Global Planet. Change*, *55*, 257–272.
Shaw, P. T. (1991), The seasonal variation of the intrusion of the Philippine Sea water into the South China Sea, *J. Geophys. Res.*, *96*(C1), 821–827.
Shaw, P. T., and S. Y. Chao (1994), Surface circulation in the South China Sea, *Deep Sea Res., Part I*, *41*, 1663–1683.
Sprintall, J., A. L. Gordon, P. Flament, and C. L. Villanoy (2012), Observations of exchange between the South China Sea and the Sulu Sea, *J. Geophys. Res.*, *117*, C05036, doi:10.1029/2011JC007610.
Tang, D. L., H. Kawamura, H. Doan-Nhu, and W. Takahashi (2004), Remote sensing oceanography of a harmful algal bloom off the coast of southeastern Vietnam, *J. Geophys. Res.*, *109*, C03014, doi:10.1029/2003JC002045.
Tomita, T., and T. Yasunari (1996), Role of the northeast winter monsoon on the biennial oscillation of the ENSO/monsoon system, *J. Meteorol. Soc. Jpn.*, *74*, 399–413.
Volkov, D. L., G. Larnicol, and J. Dorandeu (2007), Improving the quality of satellite altimetry data over continental shelves, *J. Geophys. Res.*, *112*, C06020, doi:10.1029/2006JC003765.
Wallcraft, A. J., E. J. Metzger, and S. N. Carroll (2009), Software design description for the hybrid coordinate ocean model (HYCOM) Version 2.2, *Tech. Rep. NRL/MR/7320-09-9166*, Nav. Res. Lab., Stennis Space Cent., Miss.
Wang, B., R. Wu, and X. Fu (2000), Pacific–East Asian teleconnection: How does ENSO affect East Asian climate?, *J. Clim.*, *13*, 1517–1536.
Wang, B., F. Huang, Z. Wu, J. Yang, X. Fu, and K. Kikuchi (2009), Multi-scale climate variability of the South China Sea monsoon: A review, *Dyn. Atmos. Oceans*, *47*, 15–37.
Wang, C., W. Wang, D. Wang, and Q. Wang (2006), Interannual variability of the South China Sea associated with El Niño, *J. Geophys. Res.*, *111*, C03023, doi:10.1029/2005JC003333.
Wang, G., J. Su, and P. C. Chu (2003), Mesoscale eddies in the South China Sea observed with altimeter data, *Geophys. Res. Lett.*, *30*(21), 2121, doi:10.1029/2003GL018532.
Wang, G., D. Chen, and J. Su (2006), Generation and life cycle of the dipole in the South China Sea summer circulation, *J. Geophys. Res.*, *111*, C06002, doi:10.1029/2005JC003314.
Wang, G., C. Wang, and R. X. Huang (2010), Interdecadal variability of the eastward current in the South China Sea associated with the summer Asian monsoon, *J. Clim.*, *23*, 6115–6123.
Wielicki, B. A., B. R. Barkstrom, E. F. Harrison, R. B. Lee III, G. Louis Smith, and J. E. Cooper (1996), Clouds and the Earth's radiant energy system (CERES): An earth observing system experiment, *Bull. Am. Meteorol. Soc.*, *77*(5), 853–868.
Wu, C. R., P. T. Shaw, and S. Y. Chao (1999), Assimilating altimetric data into a South China Sea model, *J. Geophys. Res.*, *104*(C12), 29,987–30,005.
Wyrtki, K. (1961), Physical oceanography of the Southeast Asian waters, *Naga Rep.*, *2*, 195.
Xie, S.-P., Q. Xie, D. Wang, and W. T. Liu (2003), Summer upwelling in the South China Sea and its role in regional climate variations, *J. Geophys. Res.*, *108*(C8), 3261, doi:10.1029/2003JC001867.

Xie, S.-P., C. H. Chang, Q. Xie, and D. Wang (2007), Intraseasonal variability in the summer South China Sea: Wind jet, cold filament, and recirculations, *J. Geophys. Res.*, *112*, C10008, doi:10.1029/2007JC004238.

Xie, S.-P., K. Hu, J. Hafner, H. Tokinaga, Y. Du, G. Huang, and T. Sampe (2009), Indian Ocean capacitor effect on Indo-western Pacific climate during the summer following El Nino, *J. Clim.*, *22*, 730–747.

Yeh, S. W., J. S. Kug, B. Dewitte, M. H. Kwon, B. P. Kirtman, and F. F. Jin (2009), El Niño in a changing climate, *Nature*, *461*, 511–514.

Zhai, F., and D. Hu (2013), Revisit the interannual variability of the North Equatorial Current transport with ECMWF ORA-S3, *J. Geophys. Res. Oceans*, *118*, 1349–1366, doi:10.1002/jgrc.20093.

Zhuang, W., S.-P. Xie, D. Wang, B. Taguchi, H. Aiki, and H. Sasaki (2010), Intraseasonal variability in sea surface height over the South China Sea, *J. Geophys. Res.*, *115*, C04010, doi:10.1029/2009JC005647.

Zhuang, W., B. Qiu, and Y. Du (2013), Low-frequency western Pacific Ocean sea level and circulation changes due to the connectivity of the Philippine Archipelago, *J. Geophys. Res. Oceans*, *118*, 6759–6773, doi:10.1002/2013JC009376.